Mon. Not. R. Astron. Soc. **000**, 000–000 (0000) Printed 26 March 2013 (MN LaTeX style file v2.2)

SCUBA-2: iterative map-making with the Sub-Millimetre User Reduction Facility

Edward L. Chapin[1,2⋆], David S. Berry[2], Andrew G. Gibb[1], Tim Jenness[2], Douglas Scott[1], Remo P. J. Tilanus[2,3], Frossie Economou[2]†, Wayne S. Holland[4,5]

[1] *Dept. of Physics & Astronomy, University of British Columbia, 6224 Agricultural Road, Vancouver, B.C. V6T 1Z1, Canada*
[2] *JointAstronomy Centre, 660 N. A'ohōkū Place, University Park, Hilo, Hawaii 96720, USA*
[3] *Netherlands Organisation for Scientific Research, Laan van Nieuw Oost-Indie 300, NL-2509 AC The Hague, The Netherlands*
[4] *UK Astronomy Technology Centre, Royal Observatory, Blackford Hill, Edinburgh EH9 3HJ*
[5] *Institute for Astronomy, University of Edinburgh, Royal Observatory, Blackford Hill Edinburgh, EH9 3HJ*

26 March 2013

ABSTRACT

The Submillimetre Common User Bolometer Array 2 (SCUBA-2) is an instrument operating on the 15-m James Clerk Maxwell Telescope, nominally consisting of 5120 bolometers in each of two simultaneous imaging bands centred over 450 and 850 μm. The camera is operated by scanning across the sky and recording data at a rate of 200 Hz. As the largest of a new generation of multiplexed kilopixel bolometer cameras operating in the (sub)millimetre, SCUBA-2 data analysis represents a significant challenge. We describe the production of maps using the Sub-Millimetre User Reduction Facility (SMURF) in which we have adopted a fast, iterative approach to map-making that enables data reduction on single, modern, high-end desktop computers, with execution times that are typically shorter than the observing times. SMURF is used in an automated setting, both at the telescope for real-time feedback to observers, as well as for the production of science products for the JCMT Science Archive at the Canadian Astronomy Data Centre. Three detailed case studies are used to: (i) explore convergence properties of the map-maker using simple prior constraints (Uranus – a point source); (ii) achieve the white-noise limit for faint point-source studies (extragalactic blank-field survey of the Lockman Hole); and (iii) demonstrate that our strategy is capable of recovering angular scales comparable to the size of the array footprint (approximately 5 arcmin) for bright extended sources (star-forming region M17).

Key words: methods: data analysis, techniques: image processing, submillimetre: general, methods: observational

1 INTRODUCTION

The Submillimetre Common User Bolometer Array 2 (SCUBA-2, Holland et al. 2013) is a new instrument for the 15-m James Clerk Maxwell Telescope (JCMT) on Mauna Kea, Hawai'i. The camera simultaneously images the sky in two broad bands centred over 450 and 850 μm, with approximately 7.5 and 14.5 arcsec full-width at half-maximum (FWHM) point spread functions (PSFs). The focal planes at each wavelength are populated with 4 rectangular subarrays, consisting of 40×32 bolometers each, and together subtend a nearly 7 arcmin × 7 arcmin footprint on the sky (excluding gaps, the continuous solid angle is about 43 arcmin^2 per focal plane). This paper describes the properties of SCUBA-2 data that are relevant for producing maps of the imaging data, and the Submillimetre User Reduction Facility, SMURF, a software package for performing the reduction written using the Starlink Software Environment (Warren-Smith & Wallace 1993; Jenness et al. 2009). The details of the instrument design, performance, and calibration are given in two companion papers: Holland et al. (2013) and Dempsey et al. (2013).

Over the last twenty years, observations in the submillimetre band (defined here to be 200–1200 μm) have helped revolutionise several important areas of astrophysics, including: discovering through blind surveys a class of mas-

---

⋆ E-mail: echapin@sciops.esa.int, Present address: XMM SOC, ESAC, Apartado 78, 28691 Villanueva de la Cañada, Madrid, Spain
† Present address: National Optical Astronomy Observatory, 950 N. Cherry Avenue, Tucson, AZ 85719, USA

sive dusty star-forming galaxies in the early ($z > 2$) Universe, now referred to as submillimetre galaxies, or SMGs; the characterisation of the early stages of star-formation by identifying the dense, cold regions in molecular clouds where stars may eventually form; and identifying debris disks around nearby stars, helping us understand the early stages of planet formation. With 10,240 nominal detectors (of which ∼70% work and are typically useful, Holland et al. 2013), SCUBA-2 is presently the largest of a new generation of multiplexed kilopixel (sub)millimetre bolometer cameras, which also includes the cameras for the South Pole Telescope (SPT, Carlstrom et al. 2011) and the Atacama Cosmology Telescope (ACT, Swetz et al. 2011), both dedicated experiments for studying anisotropies in the Cosmic Microwave Background (CMB) using similar technology, the latter of which uses the same time-domain multiplexed readout electronics as SCUBA-2 (Battistelli et al. 2008).

Submillimetre imaging cameras generally maximise sensitivity using bolometers, rather than coherent detectors, which are limited by white photon and phonon noise from the instrument and ambient backgrounds. The low-frequency noise, however, is typically dominated by sources which produce slow variations in the background (e.g., thermal variations within the cryostat, and the atmosphere for ground-based cameras), and drifts in the readout electronics. Such noise has a power spectrum $\propto 1/f^{\alpha}$ ($\alpha > 0$), and the frequency at which it is comparable to the white noise level is called the "$1/f$ knee". Since the low-frequency noise is largely correlated between all, or subsets, of the bolometers in time, it can be suppressed during map-making, since astronomical signals have the distinct property that they are fixed in a sky reference frame (assuming they are not time-varying). If successful, the noise in the resulting map is said to be "white noise limited", meaning that it is uncorrelated spatially, and has an amplitude that scales as the NEFD$/\sqrt{t}$, where the NEFD is the noise-equivalent flux-density (the white noise level of a bolometer in 1 s of integration), and t is the amount of integration time in a map pixel.

There are numerous ways to attack this map-making problem, both in terms of the data-collection method, and processing. The two most important principles to follow in terms of scan strategy are: (i) to modulate the astronomical signals of interest in such a way that they appear in the lowest-noise regions of the bolometer noise power spectrum, i.e., above the $1/f$ knee; and (ii) to provide good "cross-linking", in which each portion of the map is scanned at a range of position angles, again, to help distinguish time-varying noise features from fixed astronomical sources. In the case of SCUBA-2, (i) is achieved through fast-scanning of the entire telescope (up to 600 arcsec sec^{-1}), such that significant drift in the bolometers due to low-frequency noise occurs more slowly than the crossing times for the astronomical scales of interest; and (ii) by offering scan patterns that cross the sky at a wide range of position angles. Such methods are now used by virtually all existing ground-based submillimetre cameras (e.g., Glenn et al. 1998; Weferling et al. 2002; Wilson et al. 2008; Kovács 2008b), in preference to "chopping" methods (where the secondary is moved quickly to modulate the signal) that were more appropriate for older instruments that had poorer low-frequency noise performance, and were only sensitive to modest angular scales. We note that under some circumstances cross-linking may not be essential. For example, SPT, which was designed to measure CMB anisotropies, scans entirely in azimuth (Schaffer et al. 2011). While this strategy limits its ability to recover large angular scales transverse to the scan direction, the anisotropic filtering in its maps can be accounted for during analysis to achieve SPT's focussed objectives (in contrast, the similar ACT experiment uses cross-linking to improve its response to large-angular scales, Das et al. 2011). This approach is less practical as a general solution for SCUBA-2, however, which must serve a broader range of scientific interests.

There are three general styles of map-making that are relevant to reducing bolometer data in the literature. The simplest "direct methods" involve some basic processing of the data to remove as much noise contamination as possible, (e.g., using baseline removal and other simple filters), and then re-gridding these cleaned data into a map. Such was the basic recipe for the reduction of chopped data from SCUBA-2's predecessor SCUBA (Jenness & Lightfoot 1998; Jenness et al. 2000), and MAMBO (e.g., Omont et al. 2001), another camera from the same generation. A more recent example is the analysis of SPT data (Schaffer et al. 2011). Generally speaking, such methods are fast, although depending on the science goals and noise properties of the data, they may not achieve the best noise performance on the angular scales of interest. A method for reducing data in fields of faint point sources with Bolocam (e.g., Laurent et al. 2005), and its younger sibling the Aztronomical Thermal Emission Camera (AzTEC, e.g., Scott et al. 2008), is principal component analysis (PCA) cleaning. A statistical "black-box" removes the most correlated components of the bolometer signals, enabling the detection of point-sources close to the theoretical white-noise limits of the detectors, with reasonable computation times when small numbers of bolometers are involved (hundreds rather than thousands of detectors). However, PCA cleaning is not a good solution for producing maps of extended structures, since such sources produce correlated signals amongst many detectors, and are removed by this procedure (an exception is the iterative PCA approach of Aguirre et al. 2011). Furthermore, in the case of SCUBA-2, performing PCA on even a single subarray (typically ∼900 detectors) can be prohibitively slow.

The best existing map-making strategies for recovering information on all angular scales are maximum likelihood techniques, in which the time-series data are expressed as a sampling of the "true" map of the sky plus noise, and then the equation is inverted to estimate the map as some weighted linear combination of the data that minimizes the variance. The first good description of this method appears in Janssen & Gulkis (1992) for the production of maps from the COsmic Background Explorer (COBE – the description is relevant despite the fact that it used a differential radiometer instead of bolometers). Other descriptions in the experimental CMB literature include Tegmark (1997) and Stompor et al. (2002), and an application to data from SCUBA is described in Borys et al. (2004). The downside to such methods is that they can be both computationally expensive and have large memory requirements. While for some experimental designs fast iterative methods for the inversion do exist without requiring excessive amounts of memory, such as that of Wright et al. (1996) (which was later implemented for SCUBA by Johnstone et al. 2000), for the more general map-making problem, involving many detectors, matters are significantly complicated both by the need to measure the cross spectra for all unique pairs of bolometers, as well as performing the inversion itself. A maximum-likelihood method was successfully used to make maps from ACT data using approximately the same number of detectors as a single SCUBA-2 subarray at a single wavelength. However, the calculation is extremely resource intensive and requires a large cluster in order to run; a single map can take 10 CPU years (Fowler et al. 2010). Perhaps the most promising maximum-likelihood method that may one day be applied to SCUBA-2 data is "SANEPIC", which produced maps from Balloon-borne Large-Aperture Submillimeter Telescope data, involving hundreds of bolometers, while correctly incorporating inter-bolometer noise correlations (Patanchon et al. 2008).

The third approach adopted here for SCUBA-2 is a compromise between the previous two methods. Under the assumption that a significant portion of the (predominantly low-frequency) non-white noise sources can be modelled, an iterative solution is obtained for both the astronomical image and the parameters of the noise model. Since the remaining (non-modelled) noise sources are assumed to be white, a single scalar rms may be calculated for all of the data points from a given bolometer to characterise its noise distribution (since the noise at any instant in time is uncorrelated with others, and with the data from other bolometers), greatly simplifying the inversion step that is so complicated in the maximum-likelihood methods. In the iterative approach memory usage scales linearly with N, the product of the number of bolometers, N_b, with the number of samples in time, N_t. The computation time is the product of the number of iterations, N_iter, with the time per iteration, t_iter. For the algorithm described in this paper, N_iter is typically in the range ∼5–100 (depending on the S/N of large-scale structures, and the size of the map), and t_iter scales as $N_\mathrm{t} \log N_\mathrm{t}$, since Fast Fourier Transforms (FFTs) of the time-series are typically performed. By comparison, the fastest maximum-likelihood methods that account for inter-bolometer correlations have an execution time with an N_b^2 dependence, although it is possible to limit memory usage to be linear in N_t (e.g., Patanchon et al. 2008).

Iterative approaches to map-making have a long history in the submillimetre, such as the pipeline recipe for fitting and removing baseline drifts in SCUBA scan-map data as the astronomical image estimate improved (Jenness & Economou 1999). The closest modern relatives are the Comprehensive Reduction Utility (CRUSH, Kovács 2008a) for the Submillimeter High-Angular Resolution Camera 2 (SHARC-2), the pipeline developed for the Bolocam Galactic Plane Survey (Aguirre et al. 2011), and the Bolometer array data Analysis software (BoA) for the Large APEX BOlometer CAmera (LABOCA, Schuller 2012).

A reasonable model for correlated noise in SCUBA-2 is a single "common-mode" signal seen by all of the bolometers. Iterative estimation and removal of this signal significantly lowers the $1/f$ knee, without compromising structures on angular scales smaller than the array footprint. Residual independent drifts at lower frequencies are removed with an iterative high-pass filter. This strategy enables SMURF to reduce data on time scales commensurate with the observing times (or significantly faster), on single high-end desktop computers. For reference, all of the data analysis in this paper was performed on a machine with a 64-bit 8-core central processing unit operating at 2.7 GHz, and 48 Gb of memory. SMURF has been successfully used as part of a real-time pipeline (based on the Observatory Reduction and Acquisition Control - Data Reduction system, or ORAC-DR, Gibb et al. 2005; Cavanagh et al. 2008) offering feedback to observers at the telescope. The pipeline is also used to generate products for the JCMT Science Archive (Economou et al. 2011) hosted by the Canadian Astronomy Data Centre (CADC).

This paper is organized as follows. We first describe the properties of SCUBA-2 data, including a principal component analysis to reveal correlated noise features, in Section 2. Next, the details of the SMURF algorithm (pre-processing steps and the iterative solution) are given in Section 3. The paper is concluded in Section 4 with three detailed test cases that span the majority of observation types likely to be undertaken with SCUBA-2, with an emphasis on the mitigation of divergence problems, and characterising the output maps: (i) Uranus, a bright, compact source (Section 4.1); (ii) the Lockman Hole, a blind survey of faint point-like sources (Section 4.2); and (iii) the star-forming region M17, including bright, extended emission (Section 4.3). All of the data analysed in this paper are publicly available through the CADC SCUBA-2 raw-data queries page for the dates and observation numbers given in the text[1]. All of the analysis was performed using the Starlink KAPUAHI release from 2012.

2 SCUBA-2 DATA PROPERTIES

In this section we summarise how SCUBA-2 works, (Section 2.1), give examples of typical bolometers signals (Sections 2.2), discuss the impacts of magnetic field pickup (Section 2.3) and sky noise (Section 2.4), and finally use of principal component analysis to explore the correlated noise properties of SCUBA-2 data (Section 2.5).

2.1 Description of SCUBA-2

While the details of how SCUBA-2 works are described in Holland et al. (2013), and its calibration in Dempsey et al. (2013), we summarise the basic concepts relevant to map-making here.

Incoming light passes through a beam-splitter, and then bandpass filters, providing simultaneous illumination and wavelength definition of both the 450 and 850 µm focal planes. Each focal plane is populated by four "subarrays" (labelled s4a–s4d at 450 µm, and s8a–s8d at 850 µm), each consisting of 32 columns and 40 rows of bolometers. The bolometers are thermal absorbers (with a response time constant of $\tau \sim 1$ ms) coupled to superconducting transition-edge sensors (TESs) for thermometry. Temperature variations in the TESs produce changing currents, and therefore varying magnetic fields, which are detected and amplified

---

[1] `http://www.cadc-ccda.hia-iha.nrc-cnrc.gc.ca/jcmt/search/scuba2`

using chains of superconducting quantum interference devices (SQUIDs), before the larger output currents are digitised. Each detector has its own SQUID for the first-stage of the amplification, but the remaining stages occur within a common chain of SQUIDs for each of the 32 columns. All 40 rows are read out in sequence at a row-visit frequency of about 12 kHz. Such a high sample rate is unnecessary to produce maps, so the data are re-sampled to approximately 200 Hz before writing to disk. This rate provides a sample every 3.0 arcsec, or approximately one third of the 450 μm diffraction-limited full-width at half-maximum (FWHM) – a typical rule-of-thumb for adequately sampling a Gaussian point spread function (PSF) – at the maximum scanning speed of 600 arcsec s^{-1}. There is an additional 41st row of SQUID readouts that are not connected to TESs. These "dark SQUIDs" track non-thermal noise sources that are common to each column's amplifier chain. The relationship between the output digitised current, I, and the input power, P, or dI/dP is established using flatfield observations immediately prior to science observations, in which the output signal is measured throughout a ramp of the pixel heaters (which provide a known input power); see Section 2.1 in Dempsey et al. (2013) and Section 5.3 in Holland et al. (2013) for more details. Finally, the conversion to astronomical flux units from power involves a correction for atmospheric extinction (primarily using the 183 GHz (1.6 mm) JCMT Water Vapour Monitor to track line-of-sight opacity variations, see Section 3 in Dempsey et al. 2013), and the application of a flux conversion factor (FCF) which is established from regular measurements of calibrators such as Uranus (Section 5 in Dempsey et al. 2013).

In addition to uncorrelated white noise, and low-frequency (and often correlated from bolometer to bolometer) $1/f$ drifts, bolometer power spectra exhibit a roll-off at frequencies approaching Nyquist, which is due to the anti-aliasing filter that forms part of the 200 Hz re-sampling stage. This anti-aliasing filter also introduces an effective lag of ∼6 ms. Adding this lag to the ∼1 ms thermal time constant, as well as a negative shift of about −2.5 ms caused by a half-sample offset due to the synchronization between the pointing and bolometer data, yields a net lag of approximately 4.5 ms. There are also line features in the spectra that are thought to be produced primarily at frequencies far above the final 200 Hz sample rate, which are aliased to lower frequencies during the multiplexed readout stage before they can be removed by the anti-aliasing filter.

We note that the noise performance of SCUBA-2 has evolved over time. An initial "SCUBA-2 shared-risk observing" period (S2SRO) took place during February and March 2010, during which each of the 450 and 850 μm focal planes were populated with single subarrays, s4a and s8d, respectively. In addition to having significantly fewer available bolometers than the current fully-commissioned instrument (and therefore a mapping speed reduced by a factor of ∼4), instabilities in the fridge led to a large oscillating signal with a period of about 25 s that was correlated amongst the detectors. After upgrading and commissioning the instrument, a servo using newly added thermometers in the focal planes has effectively mitigated this problem (Section 2.5 in Holland et al. 2013). In addition, there were improvements to the magnetic shielding (reducing magnetic field pickup, as described in Section 2.3), as well as more effective removal of aliased noise sources (which has reduced both the presence of line features and the mean white noise level).

In order to reduce the impact of low-frequency noise on the final maps, SCUBA-2 scan strategies have been designed to provide: (i) good cross-linking (visiting every point of the mapped area at different scan angles); and (ii) minimal accelerations to reduce turn-around overheads (which could be quite large given the 600 arcsec s^{-1} maximum scan speed). For areas larger than the array footprint a rectangular "PONG" pattern is used, in which the boresight travels in approximately straight lines and "bounces" off the edges at 45 degree angles until the area is uniformly filled in. It is also usually combined with a rotation through a number of fixed position angles to create a "rotating PONG" with even better cross-linking. For smaller areas (of order the array footprint, or point sources), in which the PONG turn-around overheads would be large, a "constant velocity daisy" (CV Daisy) is used. Here the telescope moves in a circle, whose centre also slowly traces out a small circle. For a more complete description of the SCUBA-2 observing modes, see Section 5 in Holland et al. (2013) and also Kackley et al. (2010).

2.2 Typical bolometer signals

In Fig. 1 we show sample time-series from single bolometers in each of the 450 and 850 μm focal planes, as well as variations in the mixing chamber temperature (though not located in the focal plane itself, it is certainly correlated with the temperature of the detectors), the line-of-sight atmospheric opacity as derived from the JCMT water vapour monitor (WVM), and the telescope pointing, for two data sets, before and after the upgrades that followed S2SRO.

In the S2SRO data (Fig. 1a), observation 29 on 2010 March 13, both bolometers share significant long-timescale structure ($\gtrsim 10$ s) that appears to be related to variations in the fridge base temperature, although the similarity is clearly greater at 850 μm. Note that the total power in the fluctuations at 450 μm are comparable to those at 850 μm as one might expect if there is a comparable varying thermal load from the fridge at each wavelength that dominates. We also note that there is no obvious strong correlation between the low-frequency signal structure, at either wavelength, with the telescope motion. However, there is a suggestion that the shorter-timescale behaviour of the opacity is anti-correlated with the elevation, as expected.

The low-frequency signal component of the S2SRO bolometer output is also highly correlated amongst bolometers in the same subarray. We have calculated a common-mode signal, $\mathbf{c}(t)$, as the average time-series of all the working bolometers. We then fit the amplitude of $\mathbf{c}(t)$ at each wavelength to the signals shown in Fig. 1 and remove it, yielding the grey residual signals. These residuals are nearly white, although still with noticeable long-timescale variations. The white noise is greater at 450 μm as one would expect from the larger backgrounds compared to 850 μm.

Data from the fully commissioned instrument, observation 38 on 2011 November 12, are shown in Fig. 1b. Having solved the fridge oscillation problem, these data no longer exhibit a correlation with the mixing chamber (however, note that variations are still seen in the mixing chamber signal; such variations do not necessarily reflect changes in

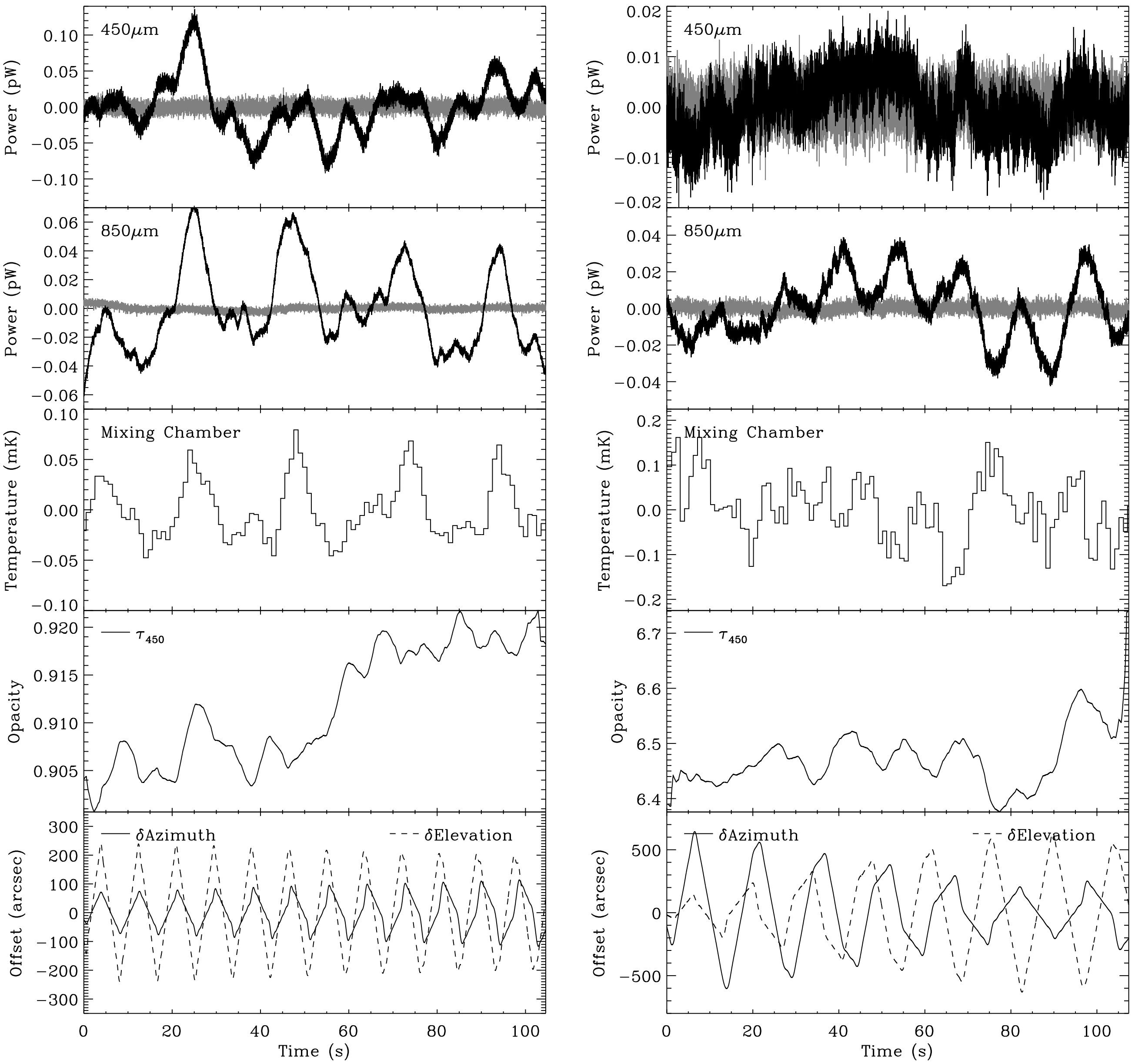

(a) S2SRO

(b) fully-commissioned

Figure 1. A comparison between single bolometer time-series in each of the 450 and 850 µm bands with the mixing chamber temperature, the line-of-sight 450 µm opacity derived from the JCMT water vapour monitor, and azimuth/elevation pointing offsets, before and after upgrading the instrument. The grey signals over-plotted in the top two panels show the residual time-series after removing the common-mode signals. (a) Data taken during the S2SRO period, observation 29 on 2010 March 13. There is a strong correlation between the bolometers and the roughly ~25 s oscillation in the fridge, but only a minor correlation with the opacity and telescope motion. The nearly flat common-mode subtracted signals show: (i) that most of the low-frequency signal is common to all of the bolometers; and (ii) the non-correlated, and predominantly white noise at 450 µm is significantly larger than at 850 µm. (b) Data taken with the fully-commissioned instrument, observation 38 on 2011 November 12. Unlike the S2SRO data, there is no strong signal produced by variations in the fridge temperature. The 450 µm data have minimal correlated low-frequency noise (as evidenced by the lack of a difference between the raw and common-mode subtracted signals), although the 850 µm data show a common signal correlated with the opacity and telescope motion (note that this scan has a significantly larger amplitude than the S2SRO data set), mostly likely caused by a combination of changing airmass (anti-correlated with opacity), and magnetic field pickup (see Section 2.3 and Fig. 3).

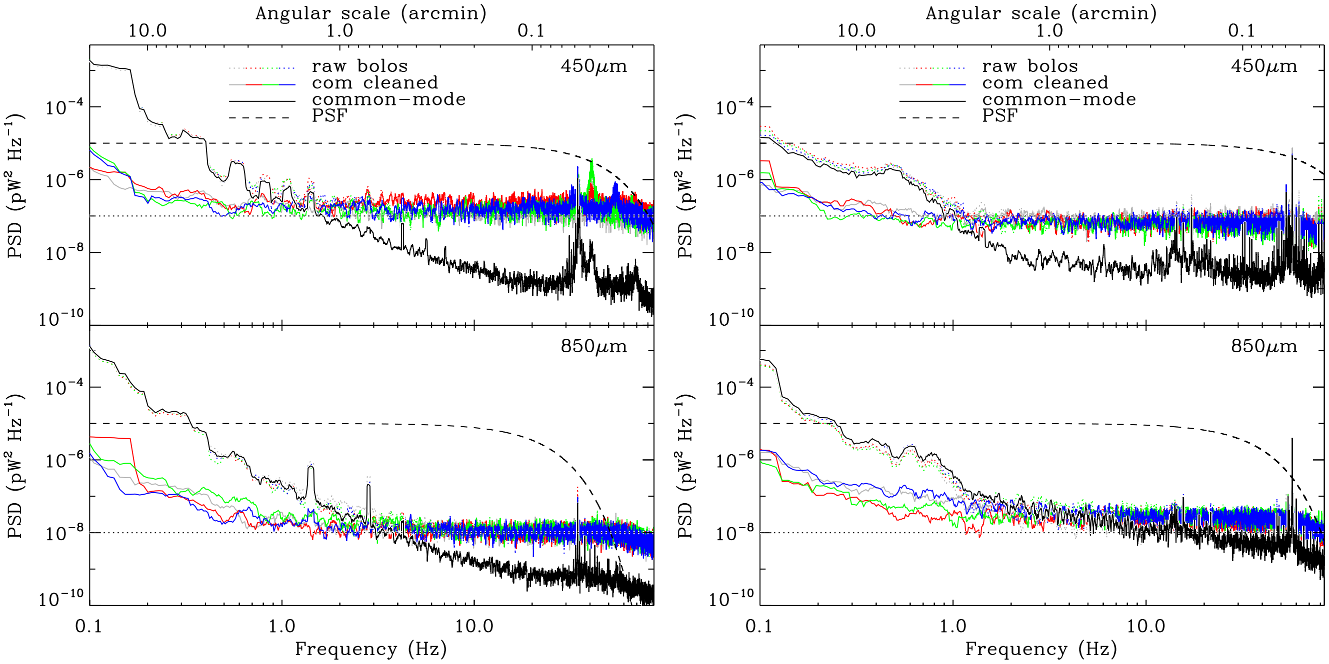

(a) S2SRO **(b) fully-commissioned**

Figure 2. Bolometer power spectral densities (PSDs) for the same two data sets (before and after upgrades) used in Fig. 1. The PSDs have been boxcar smoothed with a width of 0.1 Hz to reduce the noise slightly and clarify some features. Four of the most sensitive bolometers have been selected at each wavelength, and the flat-fielded and step-corrected (but otherwise raw) PSDs are shown as coloured dotted lines (the blue signals are for the same time series as those shown in Fig. 1). The solid black lines are the PSDs of the common-mode signals at each wavelength, and the solid coloured lines show the PSDs of the bolometers once the common-mode is removed. Finally, the dashed black lines show the spectral shape produced by a point source given the scan speeds for the two observations (120 arcsec s^{-1} in (a), and 190 arcsec s^{-1} in (b); for reference, the top horizontal axes shows the conversion from frequency to angular scale. Horizontal dotted lines at 10^{-7} and 10^{-8} pW Hz^{-1} at 450 and 850 µm, respectively, are provided as a visual reference for the white-noise levels. In addition to $1/f$ and white noise components, and line features, all of the PSDs exhibit the gradual roll-off of the anti-aliasing filter just below the Nyquist frequency. (a) For the S2SRO data, particularly at 450 µm, there are broad line features in the PSDs at both wavelengths above ∼35 Hz. At lower frequencies, the bolometer signals exhibit clear $1/f$ knees at approximately 2 and 3 Hz at 450 and 850 µm. Common-mode subtraction removes most of the correlated fridge oscillation signal, lowering the $1/f$ knees to approximately 0.6 and 1.0 Hz at 450 and 850 µm, respectively. (b) Data from the fully-commissioned instrument tend to have lower $1/f$ knees, and fewer line features. For this example, the improvement is most striking at 450 µm where the PSD is approximately two orders-of-magnitude lower in the fully-commissioned data at 0.1 Hz. The white noise performance, however, is similar for the two subarrays (s4a and s8b) that were used both before and after the upgrades.

the focal plane temperature). There is minimal correlated low-frequency noise in these 450 µm data, resulting in little difference between the raw and common-mode subtracted data. The 850 µm channel, however, exhibits a more significant signal that is obviously correlated with the telescope motion. It is also correlated amongst many of the detectors, and common-mode removal corrects it to a large extent. Part of the reason that this is seen here, and not in the S2SRO data set shown, is that the amplitude of the scan pattern is larger. This “scan-synchronous” noise is attributed to a combination of magnetic field pickup, as described in Section 2.3, and sky brightness variations due to changes in elevation (not to be confused with underlying changes in the atmosphere; a homogeneous atmosphere will appear brighter with increasing airmass). Also similar to the S2SRO data, an anti-correlation between the opacity and elevation is apparent.

Next, in Fig. 2 we produce power spectral density (PSD) plots for four of the most sensitive bolometers from both focal planes, using the same two data sets. To produce this figure, we follow the convention that the PSD as a function of frequency, $\mathbf{P}(f)$, is normalised such that the integral over frequency gives the same variance as the time-series variance across the full time-series. In other words, given a bolometer signal $\mathbf{b}(t)$,

$$\langle \mathbf{b}^2(t) \rangle = 2 \int_0^{f_\mathrm{N}} \mathbf{P}(f) df, \qquad (1)$$

where we only integrate over the positive frequencies up to f_N, the Nyquist frequency, and the factor of 2 accounts for the (equal) power that appears at negative frequencies in the discrete Fourier Transform. The units of the PSD written in this form are $\mathrm{pW}^2\,\mathrm{Hz}^{-1}$.

The dotted coloured lines in Fig. 2 show the PSDs for raw, though flat-fielded and step-corrected (Section 3.1.3) data. At each wavelength, and in both data sets, there are clear $1/f$ knees at frequencies ranging from roughly 1 to 2 Hz, followed by a predominantly white spectrum punctuated by line features at higher frequencies, and finally a roll-off caused by the anti-aliasing filter above $\gtrsim 70$ Hz. The correlation between the low-frequency components of the different bolometer signals is large. The solid black lines in Fig. 2

indicate the PSDs of the common-modes $\mathbf{c}(t)$ at each wavelength, which reproduce much of the low-frequency structure, as well as some of the higher-frequency line features. The $\mathbf{c}(t)$ otherwise drop substantially below the individual bolometer PSDs at high frequency, as expected if the bolometers are dominated by uncorrelated white noise in that part of the spectrum. The common-mode signals are fit to each bolometer time series and removed as in Fig. 1, and the resulting PSDs are shown as solid coloured lines. For reference, the top horizontal axes have been converted to angular scale assuming the scan speeds of each observation (120 arcsec s^{-1} in Fig. 2a, and 190 arcsec s^{-1} in Fig. 2b). The power spectra of unresolved point-sources are also shown as dashed lines in each band (arbitrarily normalised), showing that the smallest features resolvable by the telescope are only minimally affected by the excess noise in the line features at these scan speeds (this may not be the case at higher scan speeds).

In the S2SRO data (Fig. 2a), the low-frequency noise is very correlated between the detectors (note the tight scatter in the dotted coloured lines, and their resemblance to the common-mode), due to it being dominated by the fridge oscillations. Common-mode subtraction is very effective, reducing the $1/f$ knees in both wavelengths by about a factor of 5.

Raw data from the fully-commissioned instrument (Fig. 2b) generally have less significant $1/f$ noise as compared with the S2SRO data, and it is considerably less correlated amongst detectors (larger spread in the dotted coloured lines, particularly noticeable in these 450 µm data), leading to a less drastic improvement upon common-mode removal. However, since the data are less dominated by low-frequency noise to begin with, the signals generally require less aggressive high-pass filtering to produce maps, and therefore retain larger-scale structures than with the S2SRO data. Furthermore, there are generally fewer line features in the PSDs of bolometers in the fully-commissioned instrument. Finally, these two data sets illustrate that the white noise performance (NEFD) is in fact similar before and after the upgrades for these two subarrays (s4a at 450 µm, and s8b at 850 µm). The main improvements are a reduction in correlated and line noise features mentioned above, the larger number of working bolometers and field-of-view (approximately a factor of 4).

2.3 Magnetic field pickup

An additional noise source that is significant primarily for wide-area scans (and more so during the S2SRO period) is magnetic field pickup. Since the bolometer signals are detected through the amplification of magnetic fields, any additional changing fields within the instrument will add to the noise.

Example data from the 450 µm subarray s4a where pickup appears to be significant (observation 16 on 2010 February 28) are shown in Fig. 3. The time-series for two bolometers in the same column (not flatfielded) show that there is a strong signal with a similar shape, but opposite signs. This behaviour is seen across the entire array. The dark squid signal for the same columns exhibits a similar shape and amplitude. Since the dark squid has no thermal absorber or TES attached to it, this observed signal is not likely to be optical or thermal in nature (although there can be some cross-talk with the bolometers). Due to the fact that the sign of the gain in each stage of SQUID amplification is random (although the combined gain is constrained to be negative), and since magnetic field pickup is only seen at the input to the second stage, the pickup can appear with random signs for bolometers along a column, giving it a distinct signature from other common signals that always appear with the same sign.

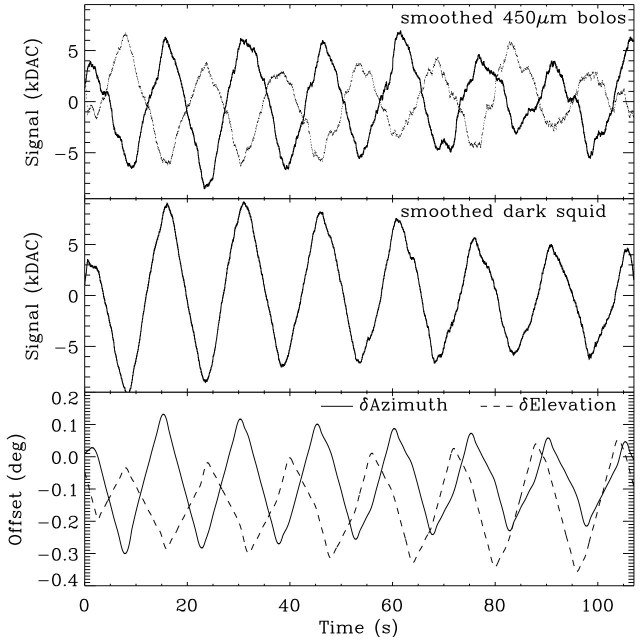

Figure 3. Evidence for significant magnetic field pickup for observation 16 on 2010 February 28 at 450 µm (s4a subarray). The top panel shows two un-flatfielded (but mean-subtracted and step corrected) bolometer time-series from the same column, with a 200 sample boxcar smoothing (approximately 1 s), illustrating that they are dominated by a similar signal with opposite signs. The second panel shows the dark squid signal for the column, also mean-subtracted and with the same boxcar smoothing. The bottom panel shows the azimuthal and elevation offsets from the map centre (mean azimuth and elevation 171.9° and 68.0°, respectively). Only the azimuthal signal is obviously correlated with the dark squids and bolometer signals, which suggests a magnetic field stationary with respect to the telescope dome as the source, since its direction with respect to the cryostat only changes with azimuthal motion.

The telescope pointing offsets for this approximately 0.5 degree diameter scan are also shown in Fig. 3. Since the phase of the azimuth offsets from the map centre in this scan pattern slowly drifts with respect to the elevation offsets, it is clear that the bolometer and dark squid signals are detecting a noise source that is correlated only with the azimuthal motion and not the elevation. This behaviour would be expected if if there were a strong magnetic field fixed with respect to the telescope dome (i.e., the earth's magnetic field). Since SCUBA-2 is mounted on a Nasmyth platform, only azimuthal motion will change the direction of such a field with respect to the cryostat. Tests have shown that, as in this example, large scans in azimuth generically produce pickup. In contrast, and as expected, changes in elevation results

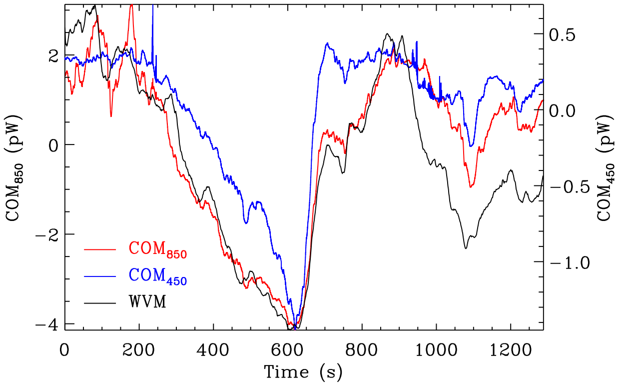

Figure 4. Illustration of the dominance of atmospheric variations on long-timescales using 35 min. of data taken in highly-variable weather conditions (line-of-sight 450 µm opacity ranging from 3.6 to 7.7) from the fully-commissioned instrument, observation 18 on 2011 March 24. Red and blue lines show the 850 and 450 µm common-mode signals, corresponding to the left- and right- vertical axes, respectively. The black line shows the line-of-sight opacity from the WVM as a proxy for atmospheric emission (arbitrary scale). Bolometer baseline drifts on timescales $\gtrsim$100 s are clearly correlated with the atmosphere in this case.

in pickup that is approximately three orders-of-magnitude smaller.

2.4 Sky noise

The data shown in Figs. 1 and 2 were taken during fairly stable weather conditions (although with different 450 µm line-of-sight opacities $\sim$0.9 and 6.5 in the S2SRO and post-upgrade data sets, respectively), and are dominated at low frequencies ($\lesssim$2 Hz) by scan-synchronous noise, rather than underlying variations in the atmosphere, or "sky noise". However, only $\sim$100 s of data were analysed. In Fig. 4, an order-of-magnitude longer (fully-commissioned) data set is plotted from observation 18 on 2011 March 24, during highly variable weather conditions (450 µm line-of-sight opacities ranging from 3.6 to 7.7, scaled from the WVM data which are shown as a black line). Unlike the earlier plots, it is clear that the bolometer baseline drifts on timescales $\gtrsim$100 s are tightly correlated with the atmospheric opacity, which serves as a proxy for atmospheric emission. The weaker correlation between the WVM and the 450 µm bolometers is probably due to the atmosphere being more transmissive at 850µm, therefore the emission detected at 450 µm comes from water vapour that is closer to the telescope than that observed at the longer wavelengths.

While the relative importance of sky noise at low frequencies is highly time- and scan pattern-dependent, in general it does not have a major impact on map-making. Upon common-mode removal (which is an integral part of our map-making strategy) uncorrelated noise remains (e.g., solid lines in Fig. 2). As we will see in Section 2.5 and 3.2.6, this remaining noise does not have a smoothly-varying correlation pattern across the focal plane as one might expect if it were due to resolved "clouds" of atmospheric emission. A high-pass filter with an edge frequency in the range $\sim$0.1–1.0 Hz is usually employed to remove this residual noise (Section 3.2), and will also remove any sky noise that is not already subtracted by the common-mode.

2.5 Principal component analysis

A method that has been used to remove correlated noise as part of the map-making procedure for Bolocam and AzTEC is Principal Component Analysis (PCA, Laurent et al. 2005; Scott et al. 2008; Perera et al. 2008). Here we use PCA to further explore correlated signals in SCUBA-2 data.

The basic method is as follows: (i) a covariance matrix is built up for all pairs (i, j) of the N bolometer time-series, $\langle \mathbf{b}_i(t), \mathbf{b}_j(t) \rangle$; and (ii) a singular value decomposition identifies a new set of statistically uncorrelated basis vectors, $\xi_i(t)$ (i.e., whose covariance matrix is diagonal), such that each of the bolometer time-series is a linear combination of the basis vectors, or components i.e., $\mathbf{b}_i(t) = \bar{\xi}\lambda_i^{\mathrm{T}}$, where each row of the matrix $\bar{\xi}$ is a basis vector, and λ_i^{T} is a column vector containing the corresponding amplitudes. The $\xi_i(t)$ are normalised by $[\sum_t \xi_i^2(t)]^{1/2}$, such that the amplitude of each component is proportional to its rms. In the earlier analyses mentioned, the low-frequency noise is assumed to be encapsulated in those components with the largest eigenvalues. Removing the projection of the time series along those components then significantly reduces $1/f$ noise while retaining most of the (higher-frequency) signal in point-like sources

A novel feature of our SCUBA-2 analysis is that we can perform PCA with 450 and 850 µm data simultaneously, potentially helping us to differentiate thermal and optical noise signals (e.g., from the atmosphere) that might appear in both wavelengths, from other noise sources that are restricted to single subarrays (such as readout noise). In Fig. 5 we show the results for a combined analysis of the s4a and s8b subarrays for the first $\sim$100 s of the same observation that was used in Figs. 1b and 2b. The nine most significant components are shown (ranked by the mean amplitudes across all working bolometers in both bands). The top and middle panels for each component show the time-series and PSDs of the normalised basis vectors. The bottom panels are maps indicating the significance (amplitudes) of the component across the focal plane (with the mean $\bar{\lambda}$ and and rms, λ_{rms}, of the amplitudes for all of the bolometers calculated separately at each wavelength also shown).

The majority of the correlated signal at both wavelengths in Fig. 5 is produced by Component 1, in which the basis vector time-series exhibits a roughly periodic signal that resembles the scan pattern in Fig. 1b. While this correlated signal appears at both wavelengths, referring to the maps of amplitudes, they are considerably stronger at 850 µm (consistent with the visual appearance of the bolometer signals in Fig. 5). Also note that the PSD for this basis vector exhibits nearly a pure $1/f$ signature with minimal line features, and no white-noise plateau (suggesting that these are high-S/N measurements of a purely low-frequency drift). Component 3 is weaker, yet also shows evidence of the scan-synchronous noise, combined with high-frequency line features that appear primarily in columns 26, 29 and 30 of the 450 µm subarray. Unlike Component 1, it is generally more dominant at 450 µm.

Why are there two components that seem to be dominated by scan-synchronous noise (which is presumably a mixture of magnetic field pickup and brightness variations

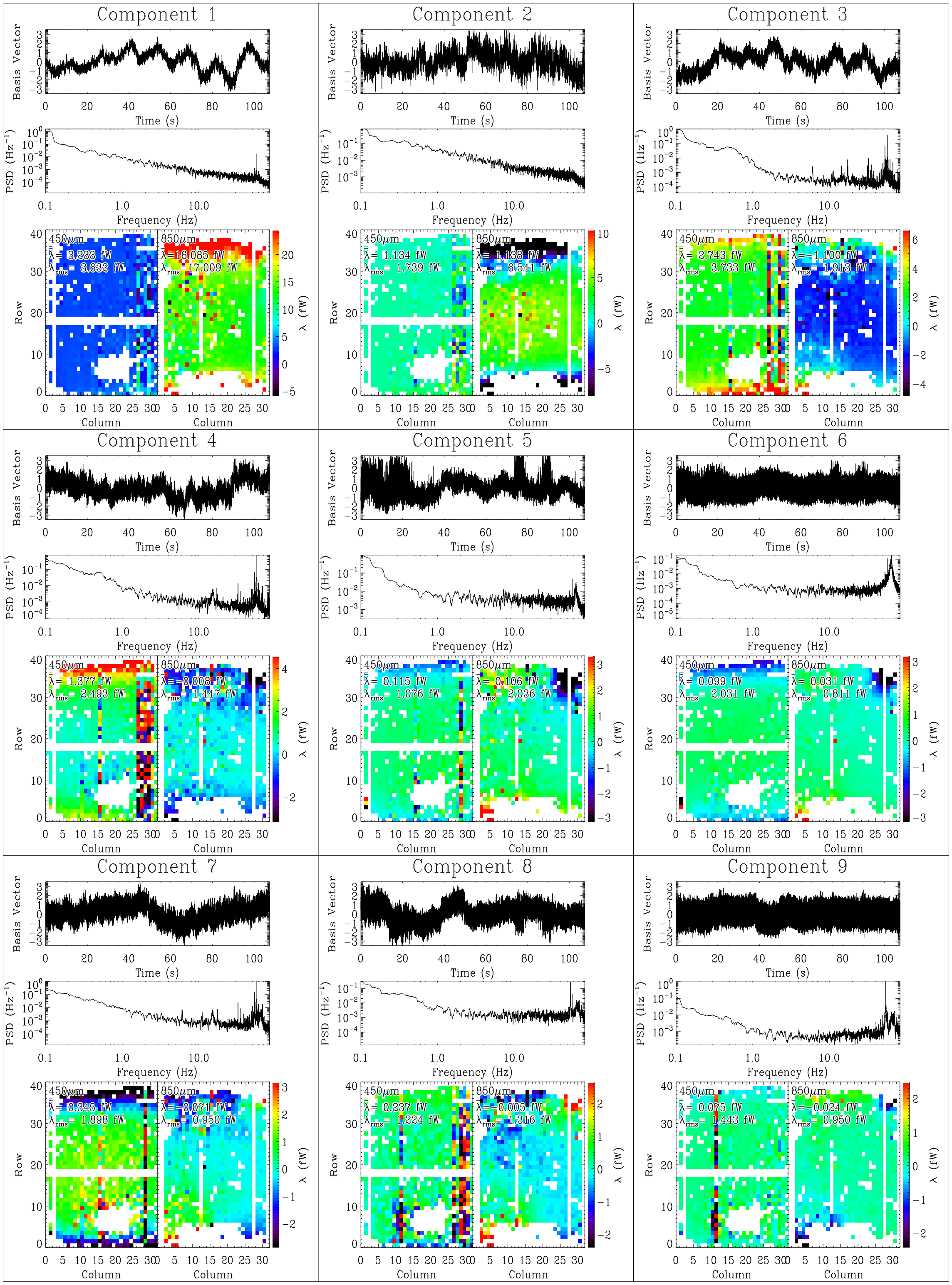

Figure 5. The first nine components from a principal component analysis, ranked by the mean amplitudes of combined 450 (s4a subarray) and 850 µm (s8b subarray) time-series bolometer data, for the same observation as that used in Figs. 1b and 2b. For each component the top plot shows the time-series of the basis vectors normalised by their rms, the middle plot its PSD, and the bottom coloured panels the ampliudes for the bolometers at each wavelength (the contribution of the basis vectors to the time-series). For reference, both the mean, $\bar{\lambda}$, and rms, $\lambda_{\rm rms}$, amplitudes for the bolometers in each subarray are also shown. Most of the correlated $1/f$ signal is encapsulated in Component 1, and appears to be dominated by scan-synchronous noise (compare with the scan pattern in Fig. 1b). Some of this signal also appears in Component 3. Component 2 is another $1/f$ signal that is dominant in the 850 µm subarray. Most of the remaining components consist of weaker $1/f$ noise and line features predominantly above ∼30 Hz. The amplitude maps show correlated patterns along columns suggesting pickup in their common amplifier chains.

in the atmosphere)? First, the smoothly-varying gradients in the amplitude maps (primarily at 850 µm) suggests that this noise has a different response across the focal plane; in this case the PCA has identified two orthogonal shapes that, when mixed in different quantities, can reproduce most of the signal in each bolometer. It is also likely that the atmospheric contribution is stronger at 450 µm (i.e., predominantly Component 3).

Like Component 1, Component 2 is a purely $1/f$ signal, with an amplitude comparable to Component 3, that appears almost exclusively at 850 µm. Since it is not obviously correlated with the telescope motion, yet has an amplitude that varies smoothly across the 850 µm subarray, it may represent the PCA's attempt to reproduce some nonlinear response to magnetic field and/or atmospheric pickup

The remaining, weaker, Components 4–9 share some common features. They all have some degree of $1/f$ noise, suggesting further residual noise related to the telescope motion and/or other slow baseline drifts. All of them also exhibit line features in their spectra, which in many cases appear at random amplitudes along columns (e.g. columns 15, and 26–30 at 450 µm in Component 4), or in a sampling of isolated bolometers (e.g. column 13, row 19 at 850 µm in Component 6). The signals that appear along columns are probably related to magnetic field pickup. Other sources of lines are thought to be aliased high-frequency noise, and also the 60 Hz mains which appear in some bolometers.

This example illustrates some of the types of correlated signals and patterns that PCA can identify in SCUBA-2 data. While there are typically one or two strong signal components detected, in general, the details can vary significantly from data set to data set, and the lengths of the time-series analysed. The reason for this is that many of the noise sources are not stationary in time (e.g., scan-synchronous noise which obviously depends on the scan pattern, and the tuning of the subarrays). It should also be clear from this example that while PCA offers some helpful insight into the various sources of noise, it does not necessarily identify clean patterns that can easily be modelled. For example, while there are clearly correlation patterns along columns as expected from the common amplification chain, the intensities of these high-frequency signals appear random in the eigenvalue maps, and a simple common-mode signal estimated from the data for each column would not remove it. Regardless, the dominant noise in excess of the fundamental white noise limit, in all cases, is at low-frequencies. This conclusion is central to our data reduction strategy described in Section 3.

3 PRODUCTION OF MAPS

The approach taken by SMURF to reducing SCUBA-2 data is to model (and remove) predominantly low-frequency noise sources that are correlated amongst detectors, and to iterate this process along with estimates of the map. Significant experimentation with different models for noise sources during SCUBA-2 commissioning required a highly flexible software framework, and a configurable user interface. To achieve this goal, while minimizing development time, it was decided to build SMURF as a Starlink package (Jenness et al. 2009), which provides access to a large suite of libraries (including a commanding and messaging interface, astrometric coordinate conversions and generation of standard WCS information, file formats etc.). Furthermore, Starlink[2] is open-source[3] (distributed under the GNU General Public Licence v3), and already used extensively at the Joint Astronomy Centre (host of the JCMT) for many other systems (Jenness & Economou 2011), which helps with interoperability. Though originally written in FORTRAN, many of the core Starlink libraries are now ported to native C, or at least have a C interface. It was therefore decided to develop SMURF in C as well (rather than C++, for example, which would have required adding further dependencies to Starlink), although we have taken an object-oriented approach. For example, all of the data for a given signal component model are encapsulated in a C structure, and there is a standard interface for all functions that handle models (member data and functions for the class, respectively). In this way it is easy to extend SMURF with new models. Parallelisation is incorporated in the most time-consuming low-level routines using threads (e.g., performing Fast Fourier Transforms, re-gridding the data), usually handling either independent blocks of bolometers, or blocks of time, in each thread, depending on the nature of the calculation. We have found that for typical data sets the processing time scales well with the number of central processing unit (CPU) cores, although beyond 8 the returns are diminished due to tasks that cannot be parallelised (e.g., reading the data from disk).

As we have seen in Sections 2.2–2.5, SCUBA-2 data are dominated at low frequencies ($\lesssim$2 Hz) by highly correlated signals. While it can be significantly reduced using simple common-mode removal (subtracting the average signal from all bolometers at each time step), the more complicated correlated residuals at these low frequencies are difficult to model. Ultimately, a very simple approach has been taken to handle both components, for which the main steps in a typical reduction are shown in Fig. 6.

First, the raw data are passed through a pre-processing stage which corrects some of the more significant glitches, applies flat-field corrections etc. Next, the iterative process begins (dashed box). Most of the low-frequency noise is removed using common-mode subtraction (`COM`,`GAI`, Section 3.2.1). Then, the extinction correction (`EXT`, Section 3.2.2) is applied. At this point the data resemble the grey bolometer traces in Fig. 1, with some residual baseline drifts still visible. These drifts are removed using a high-pass filter (`FLT`, Section 3.2.3) implemented with FFTs. The residual signal is then re-gridded to estimate the map. Finally, the map is used to estimate and remove the astronomical signal from the bolometer data (`AST`, Section 3.2.4), leaving a data set that is appropriate for measuring the white noise level of each bolometer (`NOI`, Section 3.2.5). Since the common-mode and filtering stages will have introduced ringing in the map in the vicinity of bright sources, the entire process is iterated. Each component in the dashed box of Fig. 6 is re-calculated in sequence. In this way, the second time the common-mode is calculated, for example, most of the bright astronomical sources in the data have already been removed in the previous iteration when the map was es-

---

[2] http://www.starlink.ac.uk

[3] https://github.com/Starlink

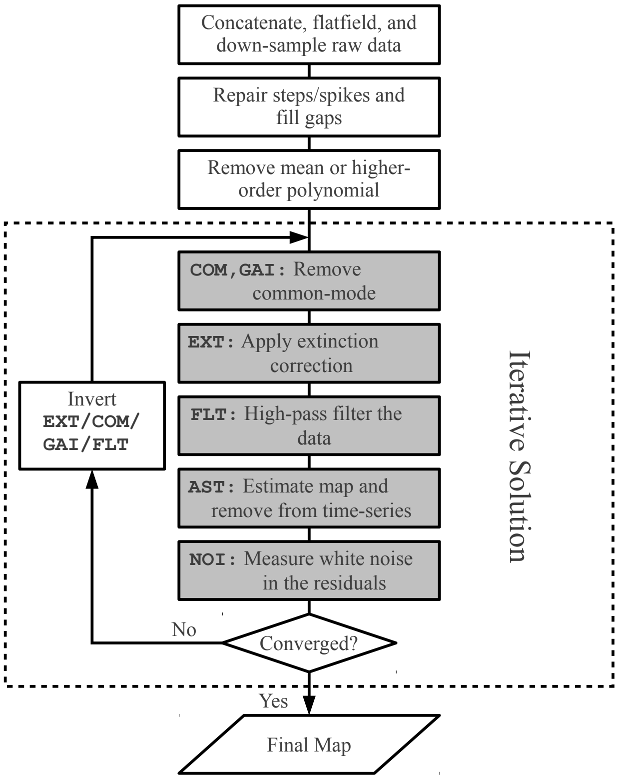

Figure 6. Typical map-making algorithm. Raw data (stored in multiple files) are read and concatenated into continuous time-series, and flatfieded. Based on the scan speed of the telescope, the data are down-sampled to match the selected output map pixel size (usually 2 and 4 arcsec at 450 and 850 µm, respectively, to ensure adequate sampling of the SCUBA-2 PSFs). A cleaning stage repairs steps and spikes, and fills gaps to ensure continuity. Finally, the mean of each bolometer time-series is removed (higher-order polynomials may also be used). The iterative portion then begins (dashed box): estimating and removing the common-mode signal (the combined `COM` and `GAI` models); applying the extinction correction (`EXT`); high-pass filtering to remove residual independent low-frequency noise (`FLT`); estimating the map by re-gridding the data, and then removing its projection from the time-series (`AST`); and finally measuring the noise in the residual time-series (`NOI`). If the solution has converged, the map is written to disk. Otherwise any multiplicative factors that may have been applied to the data are inverted (i.e., the extinction correction, `EXT`), and then the models for the low-frequency noise; the common-mode (`COM,GAI`) and high-pass filter (`FLT`). Each model is then re-estimated in turn until `AST`, at which point the previous estimate of the astronomical signal is added back into the data prior to its re-calculation.

timated, reducing the amount of ringing in the map once it is re-estimated. Note that the extinction correction is a multiplicative factor, and must be inverted prior to re-calculating any of the additive model components to preserve the data amplitude. Additive model components from the previous iteration are generically added back into the time-series immediately prior to their re-calculation. However, for the special case of the common-mode and high-pass filter stages, they are replaced simultaneously at the start of the iteration to assist with convergence (see Sections 3.3).

In general, SMURF is highly configurable, including many options for both the pre-processing stage and the iterative model components (which models are used, what order they are calculated in, how they are calculated). In Sections 3.1 and 3.2 we describe the data pre-processing steps and iterative algorithm in detail. Section 3.3 explores convergence tests and degeneracies between model components. Finally, Section 3.4 summarises the mapping performance of SCUBA-2 using SMURF.

3.1 Data pre-processing

Prior to executing the iterative part of the algorithm, the data must undergo several pre-processing steps. First, the data files are read into memory and concatenated into continuous arrays (SCUBA-2 data are broken up and written to disk every $\sim$30 s regardless of the observation length during data acquisition). As the data are loaded, they are multiplied by the flatfield correction (see Section 2.1 in Dempsey et al. 2013). Next, a series of configurable data cleaning and filtering procedures are applied; these include the removal of large glitches that may hinder the iterative solution from converging, or simply tasks that do not need to be iterated. All of the data that are flagged as bad are ignored when estimating the map.

3.1.1 Time-series down-sampling and map pixel size

The highest useful frequency in the nominally 200 Hz-sampled SCUBA-2 data is that which corresponds to the smallest angular scale that the instrument is sensitive to. As mentioned earlier, the usual rule-of-thumb for a Gaussian beam is to provide at least 3 samples for each FWHM, or roughly 2.5 arcsec for the 7.5 arcsec 450 µm channel, and 5 arcsec for the 14.5 arcsec 850 µm channel. For a typical scan speed of 300 arcsec s^{-1}, the maximum useful sample rate is therefore about 120 Hz at 450 µm, and 40 Hz at 850 µm. In order to save execution time and memory usage (both of which scale linearly with data volume), it is clearly advantageous to re-sample the data to these lower rates. In practice, the default map pixel sizes are set to 2 and 4 arcsec at 450 and 850 µm, respectively (slightly over-sampled), and down-sampling occurs as the data are loaded to match this spatial sampling given the slew speed.

The method used by SMURF is to average together multiple samples from the original time-series, x_i to estimate the lower-frequency output time-series, y_j. In general there will not be an integer number of samples from x_i in each of the y_j, so fractional samples from x_i are used at the y_j time boundaries: $y_j = (\sum w_i x_i)/(\sum w_i)$, where i runs over all the samples from x that land within, or partially overlap, y_j, and the weights, $0 < w_i \leqslant 1$, indicate the fractions of each x_i that land within y_j. The algorithm is fast since each sample in x_i need only be visited once. From a spectral point of view, this boxcar average is equivalent to applying a sinc-function low-pass filter. Such behaviour is desirable since it serves as an anti-aliasing filter; most non-white features above the Nyquist frequency in y_j that could contaminate the output data are removed.

As an alternative, we also investigated an algorithm in which the FFT of x_i is simply truncated to the target sample rate before transforming back to the time domain (i.e., applying a hard-edged low-pass filter). In practice the noise performance was indistinguishable, and required slightly longer execution time compared with the previous method, and is therefore not used.

3.1.2 Time-domain de-spiking

Spikes of short duration and high amplitude are often seen in the time series data. If not removed, they can cause ringing when filtering the data. Two alternative approaches may be used to remove these spikes. This section describes the detection and removal of spikes within the time-series of each bolometer, and Section 3.2.4 describes the iterative detection and removal of spikes as part of map estimation. In practice, map-based de-spiking usually gives superior results, and so time-domain de-spiking is switched off by default.

Each one-dimensional bolometer time-series is processed independently. At each time slice, the median value of the current bolometer is found in a box centred on the time slice, and containing a specified number of time slices (typically 50). If the residual between the time slice value and the median value is greater than some specified multiple (typically 10) of the local noise level, the time slice is flagged as a spike.

If the local noise level were estimated within the same box used to determine the median value, a spike in the box would cause the local noise level to be over-estimated severely. For this reason, the local noise level is taken as the standard deviation of the values within a neighbouring box on the "down-stream" side of the median box (that is, the side that has already been checked for spikes). In other words, the high end of the noise box is just below the low end of the median filter box. This introduces a slight asymmetry in the noise, but this should not matter unless the noise varies significantly on a time scale shorter than the box size.

This simple algorithm is not very good at distinguishing between spikes and bright point sources, and so the threshold for spike detection is usually raised when making maps of bright point sources.

3.1.3 Step correction

Sudden steps can occur in the time-series data from each bolometer, with the most likely cause being cosmic ray events (see Section 3.5.3 in Holland et al. 2013). The black curves in Fig. 7 show examples of such steps in the time-series for two bolometers. If not removed, these steps can cause severe ringing when filtering, and visible streaks in the final map, corresponding to the paths of individual bolometers over the sky.

Steps occur with a wide range of heights and shapes. The ratio of step height to noise can vary from less than 10 to several hundred. Some steps occur over a single sample, such as the step close to sample 5000 in Fig. 7b, but others happen more gradually, such as the step close to sample 5300. In addition, a step can be preceded or followed by a short period of instability, as is visible at the bottom of the step in Fig. 7a (this is probably due to the response of the SCUBA-2 anti-aliasing filter; the sudden large step occurs prior to the 200 Hz re-sampling). Further problems are caused by steps that occur close together in time, such as the large downward step followed by a smaller upward step close to sample 5000 in Fig. 7b.

Detecting and correcting such a wide variety of steps reliably has proved to be a challenge. In outline, the following stages are involved in detecting steps in a single bolometer time-series:

(i) median smooth the whole time-series;
(ii) find the gradient of the median smoothed time-series at each sample;
(iii) smooth the gradient values to determine the local mean gradient and subtract this local mean from the total gradient to get the residual gradient;
(iv) find residual gradient values that exceed 25 times the local RMS of the residual gradients;
(v) group these high residual gradients into contiguous blocks of samples;
(vi) merge blocks that are separated by less than 100 samples.

The above process produces a list of candidate steps in each bolometer time-series. Each candidate step is then verified, measured and corrected using the following procedure:

(i) the above process can misinterpret the edges of a bright source as a step, so we ignore blocks that occur close to bright sources;
(ii) if the block passes the above test, a least squares linear fit is performed to the median-filtered bolometer data just before the block, and this fit is extrapolated to predict the data value expected at the centre of the block;
(iii) a least squares linear fit is performed to the median-filtered bolometer data just after the block, and this fit is extrapolated to predict the data value expected at the centre of the block;
(iv) the difference between these two expected data values is taken as the step height;
(v) the preceding three steps are repeated several times, each time including a different selection of samples in the two least squares fits, with the mean and standard deviation of the corresponding set of step heights found;
(vi) if the mean step height is small compared to the standard deviation of the step heights, or compared to the noise in the bolometer data, then the step is ignored;
(vii) if the above checks are passed, all subsequent bolometer samples are corrected by the mean step height;
(viii) bolometer samples within the duration of the step, and a few samples on either side, are flagged as unusable.

Once all steps have been corrected within a bolometer time-series, a constant value is added to all samples in the time-series to restore its original mean value.

The results of step correction are shown by the red curves in Fig. 7. For comparison, the blue curve shows the uncorrected time-series from a nearby bolometer that does not suffer from steps. The agreement between the red and blue curves confirms that the step correction algorithm is working satisfactorily.

3.1.4 Gap filling / apodisation

SMURF uses FFTs of the bolometer data extensively for filtering. Data that have been flagged as bad for any reason

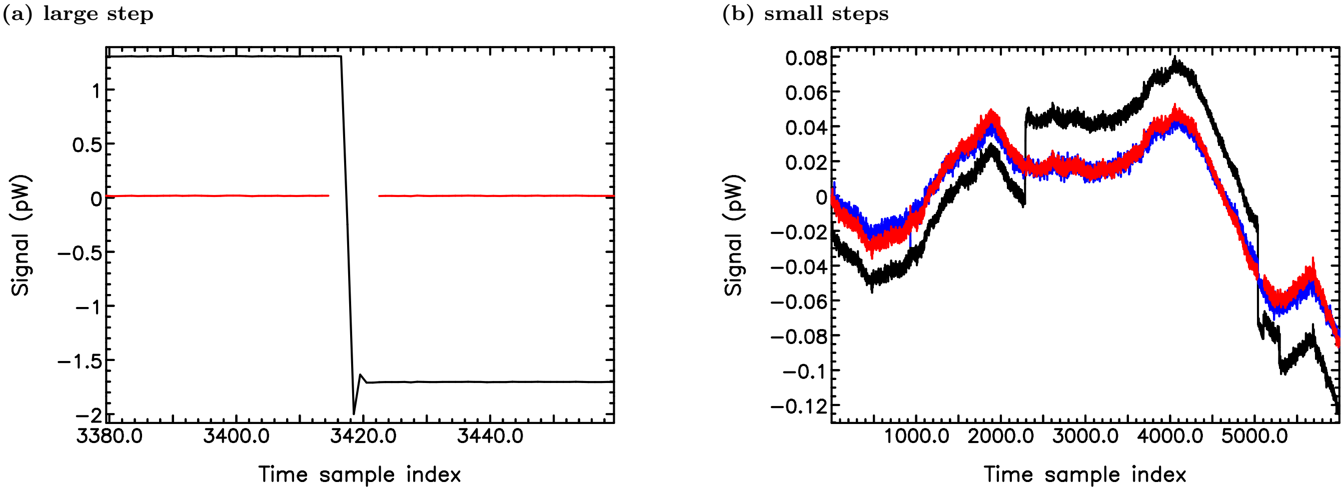

Figure 7. Examples of steps in time-series data. Steps occur with a wide range of heights from the large steps shown in (a) to the small steps shown in (b). Large steps are often followed by a brief "over-shoot" as shown in (a) which is ringing caused by the anti-aliasing filter. In both plots, the black curve is the uncorrected time-series, and the red curve is the corrected time series. Samples close to a step are omitted in the corrected time-series. In (b) the blue curve is the uncorrected time-series for a nearby bolometer. The similarity between the red and blue curves shows that the step correction is performing well.

(for instance, due to the presence of spikes, steps, or unusual common-mode signal) need to be excluded. For this reason, each contiguous block of bad data samples is filled with artificial data before taking the FFT. A least squares linear fit is performed to the 50 samples preceding the block, and a similar fit is performed to the 50 samples following the block. These are used to estimate the expected values at the start and end of the block of bad values. The bad values are then replaced by linear interpolation between the expected start and end values. Gaussian noise is added with a standard deviation equal to the mean of the RMS residuals in the two fits. These flagged and filled portions of the data are then given a weight of zero when estimating the map.

In addition to replacing bad samples before the FFT, it is also necessary to ensure that the data values at the start and end of the time-series are similar. Since an FFT treats the data as a single cycle in an infinitely repeating waveform, any large difference between starting and ending values will effectively introduce sudden steps at the start and end of each cycle, causing unwanted oscillations (ringing) in the transform. Another consequence of the cyclic nature of the FFT is that features at one end of the time series can affect the filtered values at the other end of the time series. Two methods are available to avoid these two problems:

(i) Apodisation: a number of samples at the start and end of each bolometer time-series are multiplied by a cosine function in order to roll the data values off smoothly to zero. The default number of samples modified at each end of the time-series is given by half the ratio of the sampling frequency to the lowest retained frequency, the edge frequency of the high-pass filter (Section 3.2.3). In addition, each end of the time-series is padded with double this number of zeros. This method is illustrated in Fig. 8. It is not used by default as it reduces the amount of data available for the map, and can significantly hinder very short observations (e.g., of calibrators when focussing the telescope).

(ii) Padding with artificial data: instead of padding with zeros, each time-series is padded with artificial data which connects the two ends of the data stream smoothly and includes Gaussian noise. No apodisation is performed. The number of samples of padding at each end is again equal to the ratio of the sampling frequency to the lowest retained frequency. This is illustrated in Fig. 9. See Stompor et al. (2002) for a thorough discussion of this procedure within the context of CMB map-making. This method is used by default.

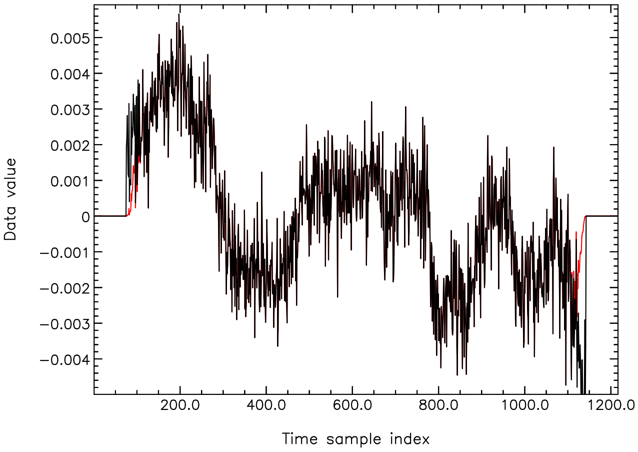

Figure 8. The black curve shows a bolometer time-series, padded with zeros. The red curve shows the time-series after apodisation.

3.1.5 Bolometer filtering

Despite the ability of the map-maker to iteratively remove many noise components, under some circumstances it may be desirable to filter the data once during the pre-processing step. Three main filtering options are available:

(i) The most commonly-used pre-processing filter is polynomial subtraction. A polynomial of the requested order is

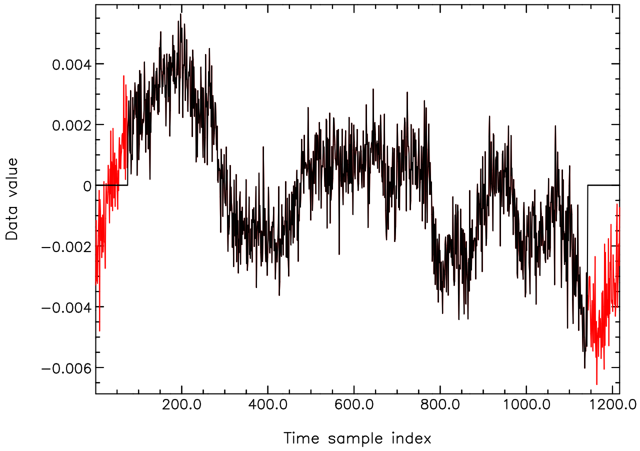

Figure 9. The black curve shows the same bolometer time-series as in Fig. 8, again padded with zeros. The red curve shows the time-series after padding with artificial data.

fit and removed from each bolometer time-series. At a bare minimum, the mean is removed from all of the bolometers (order 0) in all reductions described in this paper.

(ii) All of the filters available as part of the iterative Fourier Transform Filter (Section 3.2.3) can also be applied once during pre-processing.

(iii) As an alternative to the iterative map-making procedure, cleaning by principal component analysis (PCA) is available as an experimental pre-processing option (Section 2.5). The most significant components in the analysis are identified, and the projection of each bolometer time-series along their basis vectors are removed. A single parameter specifies the threshold on the amplitude of the components to be removed, as a number of standard deviations away from the mean value. Subarrays are cleaned independently, once, for the full length of each continuous chunk of data. Given the computational expense of this method, and initial tests which showed little improvement over simple high-pass filtering, this method has not yet been explored in detail with SCUBA-2 data. However, since systematic effects seem to come and go, it is possible that PCA could be useful for particular data sets.

3.1.6 Additional data rejection

Despite the cleaning operations described in the previous sections, the data from a given bolometer may be unusable due to it being poorly biased, having an incorrect flatfield correction applied, or having some other particularly pathological noise contamination. Most of these bolometers can be flagged simply by identifying outliers in the distribution of bolometer white noise levels. By default, SMURF measures the PSD of all bolometers between 2 and 10 Hz, after all other pre-processing steps have been run (identical to the measurement in Section 3.2.5). Despite having significant low-frequency noise (and possibly bright astronomical source) contamination, this higher-frequency portion of the PSD is generally quite flat. Furthermore, even if there is contamination, the purpose of this measurement is to identify outliers, rather than provide a meaningful absolute measurement of a given bolometer's white noise level. Both high and low (e.g., due to an incorrect and very small flatfield correction being applied) outliers from the centre of the logarithm (to reduce the impact of outliers) of the bolometer noise distribution are flagged.

Finally, data that are taken while the telescope is either moving extremely slowly, or extremely fast, are flagged and ignored when estimating the map. When the telescope is moving slowly, astronomical signals appear at low frequencies in the bolometer data that are dominated by $1/f$ noise (in the extreme case of no motion, the bolometers have zero sensitivity). When the telescope is moving significantly faster than 600 arcsec s^{-1}, both the thermal response of the bolometers, and the anti-aliasing filter in the readout electronics (Section 2.1) can significantly distort signals. The default allowable range of speed is 30–1000 arcsec s^{-1}. These thresholds primarily reject short periods when the telescope was stationary prior to commencing the scan pattern (generally speaking the speed is constant once the scan begins). The scan speed can also briefly exceed the upper limit when approaching the maximum requested speed of 600 arcsec as the pointing system struggles at high elevation.

3.1.7 Impact of lags

In principle, the effects of the bolometer thermal response, anti-aliasing filter, and data acquisition lags should be accounted for; together they produce a net lag in the bolometer signals of about 4.5 ms with respect to the pointing data (Section 2.1). This can be modelled by convolving the "pure" bolometer signals with a single system response function. Similarly, this effect could be removed using de-convolution as a pre-processing step. The impact of this lag is primarily a reduction in point-source sensitivity since scans at different position angles will detect the source at slightly different positions (and therefore reduce the peak signal once averaged together). This attenuation is most significant at 450 µm given the smaller beam size, and at the greatest scan speeds. For reference, at a speed of 150 arcsec s^{-1} (typical for CV daisies of calibrators and deep fields) the attenuation is a negligible <1% at 850 µm, and ∼1% at 450 µm. However, at the maximum speed of 600 arcsec s^{-1} (for the largest, and typically shallowest maps), this attenuation grows to about 5% and 15% at 850 and 450 µm, respectively. It is unlikely that this response has had a significant impact on observations taken to date, since such scans have been used primarily for shallow cosmology fields for which only the 850 µm data are expected to be useful, or Galactic fields of extended structures (which are less sensitive to this effect). In the present Starlink KAPUAHI release there is no option to de-convolve the system response. However, it is presently being added and will be present in future releases.

3.2 Iterative model calculation

Once the data have been cleaned, and the worst data flagged, the iterative solution for the map and contaminating noise signals begins.

First, we describe the basic model for SCUBA-2 data. We express the digitised signal observed by the ith bolometer as a function of time,

$$\mathbf{b}_i(t) = f_i[\mathbf{e}_i(t)\mathbf{a}_i(t) + \mathbf{n}_i(t)], \quad (2)$$

where $\mathbf{a}(t)$ is the time-varying signal produced by scanning the telescope across astronomical sources, $\mathbf{e}(t)$ is the time-varying extinction, which is a function of the telescope elevation and atmospheric conditions, and $\mathbf{n}_i(t)$ represents sources of noise. The two terms in square brackets, as written, have units of power delivered to the detectors (pW). The scale factor f_i converts this effective power to the digitised units recorded on disk – the flatfield multiplied by a digitisation constant (applied once during pre-processing) – which in this formulation is assumed to be constant in time.

We then express the noise, $\mathbf{n}_i(t)$, as the sum of several components,

$$\mathbf{n}_i(t) = \mathbf{n}_i^{\mathrm{w}}(t) + g_i\mathbf{n}^{\mathrm{c}}(t) + \mathbf{n}_i^{\mathrm{f}}(t), \qquad (3)$$

where $\mathbf{n}_i^{\mathrm{w}}(t)$ is uncorrelated white noise, $\mathbf{n}^{\mathrm{c}}(t)$ is a correlated or common-mode signal (with an optional scale factor g_i for each bolometer), and $\mathbf{n}_i^{\mathrm{f}}(t)$ is (predominantly low-frequency) noise in excess of the white noise level, which is either uncorrelated from bolometer-to-bolometer, or at least does not have a simple correlation relationship that would lead to it being included in $\mathbf{n}^{\mathrm{c}}(t)$.

During pre-processing, the map-maker divides by f_i once. Then, in each iteration, the map-maker models and removes $g_i\mathbf{n}^{\mathrm{c}}(t)$, divides by $\mathbf{e}_i(t)$, and applies a high-pass filter to remove $\mathbf{n}_i^{\mathrm{f}}(t)$ from the bolometer time-series. This procedure isolates the astronomical signal and white noise, $\mathbf{a}_i(t) + \mathbf{n}_i^{\mathrm{w}}(t)$, for estimating the map. Finally, once the map is estimated it is projected into the time-domain and removed from the bolometer time-series leaving $\mathbf{n}_i^{\mathrm{w}}(t)$, in which the bolometer noise can be measured. This is the most typical sequence; in practice the user can select an arbitrary order, although the solution converges much faster when the strongest components are estimated first, and then subtracted, leaving a cleaner signal for subsequent model estimates.

After the first iteration, there will almost certainly be correlated errors between the model estimates. For example, the presence of a bright astronomical source will contaminate $\mathbf{n}^{\mathrm{c}}(t)$ (which is a simple average of all of the bolometer time-series at each instant in time), leading to an over-subtraction, and in turn, negative bowls in the map.

Subsequent iterations, however, diminish such problems. Each additive model component is re-estimated in the same sequence, after first adding the previous estimate back into the time-series (but importantly, not the other components). In this case, much of the astronomical signal will have been identified and removed in the previous calculation of $\mathbf{a}_i(t)$, and therefore there will be less contamination in $\mathbf{n}^{\mathrm{c}}(t)$, and less negative bowling in the map. Any multiplicative models [e.g., $\mathbf{e}_i(t)$] are inverted immediately prior to the start of a new iteration to preserve the units of the data. The iterative solution will thus converge, barring degeneracies between model components.

The full set of model components available, and the parameters that control them, are described in the following sections. Table 1 shows the typical order in which they are calculated. For a discussion on convergence tests and degeneracies, see Section 3.3.

Table 1. Summary of the model components that can be fit to SCUBA-2 time-series data with SMURF. Only the first group of models are typically fit to the data (`COM`–`NOI`) in the indicated order. The remaining models (`DKS`–`PLN`) are usually omitted, although they are available as options.

Model	Description
`COM`	remove common-mode signal
`GAI`	common-mode scaled to each bolometer
`EXT`	extinction correction
`FLT`	Fourier Transform filter
`AST`	map estimate of astronomical signal
`NOI`	noise estimation
`DKS`	dark squid cleaning along columns
`PLN`	2-dimensional time-varying plane removal
`SMO`	time-domain smoothing filter
`TMP`	pointing as baseline template

3.2.1 `COM,GAI`: common-mode estimation

Fig. 10 shows the time-series from a selection of typical bolometers.[4] The similarity between most bolometers is evident, and forms the common-mode signal – assumed to be a consequence of variations in the atmospheric emission and fridge temperature. This common-mode usually dominates the astronomical signal for all but the brightest sources, and swamps faint extended structure. The purpose of the `COM` and `GAI` models is to remove this common-mode signal.

The `COM` model is the common-mode signal itself [$\mathbf{n}^{\mathrm{c}}(t)$ in Eq. 3]. It is a single time-series that is estimated by finding the mean of all bolometers at each time step. Bolometer values that have been flagged as unusable are excluded from the mean.

Even after flat-fielding, bolometers may have slightly varying sensitivities and so the amplitude of the common-mode variations will also vary from bolometer to bolometer. Comparing each bolometer time-series with the common-mode signal allows an estimate of the relative bolometer sensitivity to be obtained. In practice, a least squares linear fit is performed between the bolometer time-series and the common-mode to determine a gain (g_i in Eq. 3) and offset for each bolometer. The gain and offset for each bolometer is known as the `GAI` model. Each bolometer value can then optionally be scaled and shifted using these values so that all bolometers share a common (but as yet unknown) calibration. This provides an alternative (or additional) flat-fielding strategy to that described in Section 2.1.

An option exists to cater for time-varying sensitivities. In principle, the gain of the bolometers should be constant in time. However, there is evidence that there are slight variations, and this option does tend to slightly improve the noise in maps. If used, the least squares fits described above are performed on short blocks of contiguous time slices, providing multiple gain and offset values for each bolometer (one pair for each block of time slices). The gain and offset at any required time slice can then be found by interpolation between these values.

---

[4] The data have been flat-fielded and each time series has been adjusted to a mean value of zero.

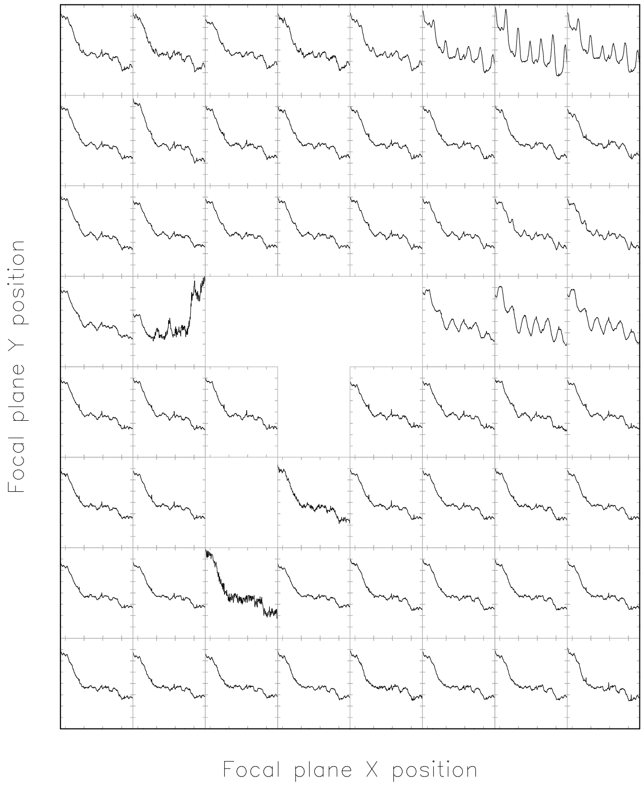

Figure 10. A selection of bolometer time-series from a representative region of the focal plane after flatfielding and removal of a constant baseline. Each sub-plot shows the power from a single bolometer over a 30 s interval. The lower and upper vertical limits of each plot are -0.02 pW and $+0.02$ pW, respectively. It can be seen that most bolometers exhibit a common time variation overlaid with other features. Empty squares indicate the locations of broken bolometers.

It can be seen from Fig. 10 that some bolometers depart radically from the common-mode, indicating some problem with the bolometer. Such bolometers are identified by calculating the Pearson correlation coefficient between each bolometer time-series and the common mode. Bolometers for which the correlation coefficient is below a specified limit, or which have unusually high or low gains compared to the other bolometers, are flagged as bad in order to omit them from the final map. If the option described above for handling time-varying sensitivities is used, then a correlation coefficient can be determined for each individual block of time slices. This allows individual bad blocks to be rejected from a bolometer time-series, rather than rejecting the whole bolometer. As a warning, rejecting data based on outlier gain values can be misleading in cases where the data are dominated by magnetic field pickup. For example, the common-mode signal for the data in Fig. 3 would resemble the azimuthal scan pattern, but clearly the gains will have opposite signs (such that one or the other bolometer would be erroneously flagged). Experimental models that were investigated for magnetic field pickup removal are described in Section 3.2.6.

The common-mode value at each time slice is calculated as the unweighted mean of the values of all bolometers that have not previously been flagged as bad for some other reason. Bolometer values that were flagged as bad simply because they were poorly correlated with the common-mode on the previous iteration are, however, included in the new common-mode estimate. If such samples are excluded, there is a strong possibility of discontinuities appearing in the `COM` model at block boundaries. These in turn can lead to ringing when filtering, and instabilities in the convergence process.

Any astronomical sources that are smaller than the array size will contribute signal to some bolometers but not other bolometers, thus biasing the simple mean used to estimate the common mode. However, on each iteration of the map-making algorithm illustrated in Fig. 6, a large fraction of the remaining astronomical signal is extracted from the bolometer time-series and transferred to the output map, resulting in subsequent estimates of the common-mode being more accurate. It is also for this reason that the previously described step of (re-)flagging outlier portions of the data is generally performed iteratively, rather than once as a pre-processing step, since bright/compact astronomical sources can be the cause of rejection in early iterations.

Any extended astronomical emission on a scale comparable to or larger than the spatial extent of the area used to estimate the common-mode will contribute a similar signal to all bolometers. Therefore such extended emission is indistinguishable from the other sources of common-mode signal (e.g., atmosphere variations) and will be removed by the `COM` model. This places a limit on the spatial extent of astronomical structure that can be recovered.

For this reason, the usual practice is to estimate a single `COM` model by examining data from all four subarrays in each waveband, since this allows spatial structure on the scale of the whole focal plane to be recovered. However, sometimes there is evidence that the common-mode differs from one array to another, and so an option exists to estimate a separate `COM` model for each individual subarray, with a consequent lowering in the scale of spatial structure that can be recovered.

3.2.2 EXT: extinction correction

The extinction correction is a multiplicative factor that is normally derived using the WVM, and is not considered to be a free parameter in the solution [$\mathbf{e}_i(t)$ in Eq. 2]. However, it is applied as part of the iterative solution, rather than a pre-processing step, since any small errors will be amplified by the large low-frequency drifts in the raw bolometer time-series. For example, if the bolometer drift is 1000 times greater than an astronomical source of interest, a 1 per cent error in the flatfield will produce stripes of order 10 times the astronomical signal amplitude in the final map! If `EXT` is applied after the bulk of the low-frequency noise has been removed (e.g., `COM,GAI`), then there is little potential for such small errors to affect the final map. For details on how it is calculated see Dempsey et al. (2013). Note that its numerical value is calculated only once, and simply applied as a scale factor in the iterative solution. Unlike the additive model components, it is inverted at the start of each iteration to preserve the amplitude of the data before the re-calculation of other model components.

3.2.3 `FLT`: Fourier Transform filter

This model takes the FFT of the bolometer time-series data, and can apply both high- and low-pass filters, as well as notch filters, at hard frequency edges specified by the user. Alternatively, the frequency edges of the filters may be defined in terms of an angular scale, but converted into a frequency through knowledge of the mean telescope slew speed. The time-series are generally gap-filled (Section 3.1.4) before the transform to avoid ringing (primarily caused by wrap-around discontinuities at the ends of the time-series). Finally, a whitening filter may also be applied in which a simple form, $1/f^{\alpha} + \mathrm{constant}$, is fit to the power spectrum of each bolometer, and then the bolometer FFT is multiplied by the square root of its inverse (though normalised to preserve the white noise level). The signals that are removed from the time-series by this process are stored in the `FLT` container array. Typically this model is used purely as a high-pass filter to remove most of the residual $1/f$ noise following common-mode removal [$\mathbf{n}_i^{\mathrm{f}}(t)$ in Eq. 3]. Low-pass filtering is redundant for two reasons: (i) SMURF already low-pass filters and re-samples to a lower sample rate, as described in Section 3.1.1; and (ii) the act of re-gridding the data to produce map estimates effectively low-pass filters the data below a frequency that corresponds to the inverse of the crossing time of a single map pixel. Notch filters have not been proven to be useful with SCUBA-2 data, particularly since line features tend to move around (i.e., a dynamic line-detection system would have to be developed, and care would have to be taken that astronomical sources are not suppressed).

3.2.4 `AST`: map estimation

Map estimation is accomplished using a nearest-neighbour resampling of the data onto a pre-defined map grid. For the ith map pixel, $\mathbf{m}(x_i, y_i)$, the brightness is estimated as the weighted average of the bolometer data samples $\mathbf{b}_j$ that land within that pixel (from any bolometer or point in time, provided that they are not flagged as bad or gap-filled, Section 3.1.4),

$$\mathbf{m}(x_i, y_i) = \frac{\sum_j \mathbf{w}_j \mathbf{b}_j}{\sum_j \mathbf{w}_j}. \tag{4}$$

For the initial iteration the weights $\mathbf{w}_j$ are set to 1, but subsequently they are set to $1/\sigma_j^{\mathbf{w}2}$, the estimated inverse variance expected from the bolometer white noise levels, as discussed in Section 3.2.5. This weighting scheme is sensible provided that the bolometer data have no correlated (e.g., low-frequency) noise.

In addition to the signal map, a variance map $\mathbf{v}(x_j, y_j)$ is estimated. The default procedure is to estimate this quantity given the scatter in the weighted samples. This is accomplished by dividing the biased weighted sample variance by the number of samples that went into the average (akin to the formula for standard error on the mean, but accounting for weights),

$$\mathbf{v}(x_j, y_j) = \frac{\sum_j \mathbf{w}_j \sum_j \mathbf{w}_j \mathbf{b}_j - \left(\sum_j \mathbf{w}_j \mathbf{b}_j\right)^2}{N\left(\sum_j \mathbf{w}_j\right)^2}, \tag{5}$$

where N_j is the total number of bolometer samples that land in the pixel. As written, this algorithm is numerically unstable if the two terms in the numerator are large, and of nearly the same value: floating point precision errors can cause the difference to be significantly incorrect. In practice we use the superior "weighted incremental algorithm" that calculates incremental differences, as described in West (1979).

We decided not to use an unbiased estimator (e.g., the extension of the common $(1/N-1)\sum_j(\mathbf{b}_j - \bar{\mathbf{b}})^2$ estimator using weights), since in practice it would require accumulating an additional array of values at every map pixel, and only results in a small difference where there are less than ~ 10 samples per pixel (a situation that is almost never encountered in a SCUBA-2 map, except in the edge pixels).

Finally, once the map estimation is complete, the map is projected into the time domain (the signal that would be produced in each bolometer by the signal represented by the map, $\mathbf{a}_i(t)$ in Eq. 2) and removed.

In addition to map estimation, the `AST` model can also be used to perform map-based despiking of the time-series. Unlike the time-domain despiker (Section 3.1.2), this calculation utilises the scatter in the population of samples that land in a map pixel (from different times and bolometers) to reject outliers. This method is more robust against false-positive detections of bright/compact astronomical sources since transient features in the time-series are unlikely to occur by chance whenever a bolometer crosses a specific location on the sky, whereas real astronomical sources are at fixed spatial locations.

The estimated variance, $\mathbf{v_p}(x_i, y_i)$, of the normalised weighted samples that land in the ith map pixel is simply the biased weighted sample variance (i.e., the variance map value multiplied by the number of samples):

$$\mathbf{v_p}(x_i, y_i) = N_i \mathbf{v}(x_i, y_i). \tag{6}$$

In order to compare the weighted differences between the samples and the map values, $[\mathbf{b}_j - \mathbf{m}(x_i, y_i)]$ to $\mathbf{v_p}$, they must be scaled appropriately. We define a normalised difference, $\mathbf{d}_j$, in such a way that the variance of this new variable gives the weighted sample variance of the underlying data points:

$$\frac{\sum_j \mathbf{d}_j^2}{N} = \frac{\sum_j \mathbf{w}_j [\mathbf{b}_j - \mathbf{m}(x_i, y_i)]^2}{\sum_k \mathbf{w}_k} \tag{7}$$

$$\Rightarrow \mathbf{d}_j^2 = \frac{N \mathbf{w}_j [\mathbf{b}_j - \mathbf{m}(x_i, y_i)]^2}{\sum_k \mathbf{w}_k}. \tag{8}$$

The map-based despiker flags those $\mathbf{d}_j$ that are further than some threshold number of standard deviations $\sqrt{\mathbf{v_p}}$ away from zero, so that they are not used in subsequent iterations.

A final option available as part of the `AST` model is to apply constraints to the map to improve convergence, which presently include setting user-specified or low-S/N regions to a value of zero for all but the final iteration. See the discussion in Section 3.3 and examples in Sections 4.

3.2.5 `NOI`: noise estimation

The primary purpose of the noise component, `NOI`, is to measure the white noise levels of each bolometer, which is approximated with a single (non-time varying) variance, $\sigma_i^{\mathbf{w}2}$. This value is then used to calculate weights for map estimation, $\mathbf{w}_i = 1/\sigma_i^{\mathbf{w}2}$. The measurement generally occurs once all of the other models have been fit and removed [i.e., once $\mathbf{n}_i^{\mathrm{w}}(t)$ from Eq. 3 is isolated].

First, the bolometer PSDs are calculated as in Eq. 1. An average white noise level is then measured from 2 to 10 Hz, a clean region of the PSD that tends to lie above the $1/f$ knee, but below the high-frequency line features for typical bolometer data (Fig. 2). Taking this constant level for $\mathbf{P}(f)$ we then calculate the expected variance of the time-series (in approximately 200 Hz samples) using Eq. 1. If the bolometer noise were produced purely by uncorrelated sources (i.e., no other long time-scale drifts), with no high-frequency line features, and without the attenuation at even higher frequencies by the anti-aliasing filter, this is the theoretical noise limit of the detectors. These measured variances are stored, and then used in subsequent iterations to weight the data points when calculating the map estimate (Section 3.2.4). They are also used for convergence tests (Section 3.3).

Since noise estimation is usually calculated as the final step in the iteration, the data at this stage have had most of the astronomical and other large, low-frequency noise signals removed. For this reason, `NOI` may optionally perform some cleaning options, such as the step fixer (Section 3.1.3) and spike detection (Section 3.1.2), which may work better with these cleaner time-series.

Finally, it should be noted that the default procedure is to calculate the white noise levels once within `NOI`, after the second iteration. The reason for fixing these values is to prevent any potential divergence in the weight estimates with iterations, and also to provide a fixed reference for the convergence tests (Section 3.3). Note that the absolute values of the noise, and therefore weights calculated by the model, are irrelevant (only their relative values matter). The reason is that the final noise in the map is measured empirically from the scatter of the weighted data points that land in each pixel (Section 3.2.4).

3.2.6 *Experimental models for the removal of magnetic field pickup and the atmosphere*

Additional models exist as options, although they are not generally used: `DKS`, the use of dark squids as a template for removing magnetic field pickup; `TMP` which uses the azimuth of the telescope also as a template for magnetic field pickup; `SMO`, which provides a time-domain smoothing alternative to the FFT-based filter model `FLT`; and `PLN`, which fits a plane to the signal distribution across the focal plane at each time slice in an attempt to remove possible coherent atmospheric sky-noise structure.

As described in Section 2.3, wide scans can produce significant magnetic field pickup that tracks the azimuthal motion of the telescope. The `DKS` model uses the dark squid signals for each column as a template that is simply scaled (gain and offset) to each bolometer time-series before removal. Unfortunately the dark squids do not work for every column (several cases in each subarray), meaning that those columns are usually discarded when producing maps. One possible remedy is to identify dead bolometers (with otherwise working TES readouts) or intentionally disconnect working bolometers, to create replacement dark readouts in those columns. This solution has not been pursued due to the limited success at removing pickup using the presently working dark squids. Another alternative model is `TMP` in which the azimuth of the telescope itself is used as the template. For both `DKS` and `TMP`, there is some success at visibly decreasing the low-frequency scan-synchronous noise in certain data sets, although often it does not (and there are also examples in which the noise is increased). In the case of `DKS`, there may simply be components of the signal seen by working detectors that are not apparent in the dark squids. Furthermore, in the case of `TMP`, the relationship between the projection of the Earth's magnetic field on the instrument and the magnitude of the pickup may not be linearly correlated as we have assumed (verified in some cases by a comparison of the azimuthal motion with working dark squid signals). In no case was the use of these models able to reduce the $1/f$ knee substantially, necessitating the continued use of `FLT` to remove the remaining low-frequency noise. Neither `DKS` nor `TMP` are typically used.

The `SMO` model uses a rolling mean or median boxcar filter to calculate the low-frequency component of the bolometer signals, which are then removed. In other words, this is an alternative to the high-pass filtering for which `FLT` is generally used. The primary reason for developing this model was to make it more robust against ringing near the ends of the time-series, or residual spikes (for which the median filtering is particularly useful). However, the de-spiking and gap-filling algorithms that we have employed (Section 3.1.4) successfully mitigate these problems, and the `FLT` model is substantially faster.

Finally, we experimented with an alternative to `COM` for removing correlated atmospheric noise. Rather than subtracting the average signal at each time slice, `PLN` fits a plane to the observed signal at each instant. We found that there was no obvious improvement (either in terms of reducing the $1/f$ knee or reducing the noise in final maps). This result is basically consistent with those from earlier instruments (e.g., the prediction for SCUBA-2 based on SCUBA data described in Chapin et al. 2002), and suggests that the angular scale of the emitting regions in the atmosphere are unresolved at the SCUBA-2 focal plane. Sayers et al. (2010), in particular, examined several different ways of modelling and removing the correlated atmospheric noise from Bolocam data at 143 and 268 GHz (also atop Mauna Kea), finding only marginal improvements by fitting a plane, or even higher-order polynomials (see their figure 10, as well as the discussion and references to earlier work in their section 4.3). In Aguirre et al. (2011) iterative PCA cleaning was used to remove the atmosphere since the simpler methods mentioned left substantial residuals in their data (similar to the SCUBA-2 data described here, although PCA cleaning is prohibitively slow in our case).

3.3 Convergence tests and model degeneracies

The map-maker will halt after a user-specified number of iterations, or once some convergence criterion has been achieved. Presently two numerical quantities are tracked after each iteration: the change in reduced chi-squared, χ^2_{r}; and the change in the map. While convergence in χ^2_{r} is not, ultimately, a good indicator of when the solution should be stopped, we discuss its calculation and properties first as an introduction to the problem of model degeneracies.

The bolometer residual variances, σ_i^2, are measured once the modelled signal components have been removed. In the early iterations, the residuals contain both white noise, and other long-timescale features. However, when the solution has converged, this signal should look white. Taking the component of bolometer variances due to white noise, $\sigma_i^{\mathbf{w}2}$ (measured from the bolometer PSDs in `NOI`, Section 3.2.5), $\chi_{\rm r}^2$ is calculated as $(1/N)\sum_i \sigma_i^2/\sigma_i^{\mathbf{w}2}$, where i runs over the N bolometers. In other words, it is the average ratio between the measured time-series bolometer variances and their white-noise levels measured between 2 and 10 Hz, and should tend to a value of ∼1 if the low-frequency noise (and any bright astronomical signals) have been successfully removed. However, this expression does not account for the degrees of freedom in the model. Clearly there are a large number of parameters that will "fit-out" some of the uncorrelated white noise, and bias this estimate of $\chi_{\rm r}^2$ low. Indeed, for a converged map, values in the range ∼0.85–0.95 are common, depending on the precise configuration parameters. Regardless of the normalisation, once the model parameterisation has been chosen, this quantity should converge to some fixed value.

Practically speaking, $\chi_{\rm r}^2$ tends to converge before the map due to model degeneracies. One simple example is the degeneracy between large-scale astronomical structures (larger than the array footprint), and the common-mode rejection step (`COM`), which will be illustrated in Section 4.1. In this case, there is a significant space of maps with spurious large-scale structures that are anti-correlated with features in the common-mode, and the solution is free to wander this space while producing flat residuals.

Instead, we typically use a map-based convergence statistic, $M_{\rm c}$, the average absolute change in the value of map pixels between subsequent iterations, normalised by the map pixel uncertainties (square root of Eq. 5), or

$$M_{\rm c}^j = \frac{1}{N}\sum_i \frac{|\mathbf{m}(x_j,y_j) - \mathbf{m}(x_{j-1},y_{j-1})|}{\sqrt{\mathbf{v}(x_j,y_j)}}, \qquad (9)$$

where i runs over the N map pixels, and j enumerates the iterations. Experimentally we found that a change in this quantity <0.05 (on average, map pixels change by <5% of the estimated map RMS in subsequent iterations) is a good point to stop, providing correspondence with what we would choose "by eye". Letting the solver run for many more iterations in several test cases yields insignificant differences.

Another major source of divergence is correlation between `COM` and `FLT`. Since `FLT` usually consists of a high-pass filter following the application of `COM`, `COM` is completely free to grow any large-scale structure at frequencies below the chosen filter edge. While such structure does not appear in the map (as it is removed by `FLT`), we found that the solution could be made to converge significantly faster by "remixing" `COM` and `FLT`. Immediately prior to the calculation of `COM`, the values of `COM` and `FLT` from the previous iteration are added back into the residual simultaneously. In this way, truly common-mode signals, even at low-frequencies, do not leak into `FLT`.

In order to control the degeneracy between low-frequency signal that is removed, and large-scale structures in the map, we have developed a simple system for constraining regions of the map devoid of sources to a value of zero for all but the final iteration in the `AST` model (Section 3.2.4). Such regions are either user-defined in advance, or can be determined from the data using a cut on S/N. This technique is explored considerably in the examples in Sections 4.1 and 4.3.

3.4 Instrument and map-making performance

From a scientific perspective, the most important goal of map-making is to efficiently use all of the available data to achieve the greatest sensitivity to astrononomical sources that the instrument is capable of. Generally speaking, only a small percentage of the data are flagged as unusable during map-making beyond the ∼70% detector yield. As an example, for the 450 µm scan of Uranus that will be presented in Section 4.1, during pre-processing: 31% of the data (1587/5120 bolometers) are flagged due to data acquisition problems (dead or deactivated bolometers, or non-linear flatfields); 0.12% of the data are flagged due to steps (including a small region about the steps, Section 3.1.3); and 0.83% of the data are flagged because the telescope was stationary (Section 3.1.6). Once the iterative solution begins: 55 spikes are detected using the map-based despiker (1.2×10^{-6} % of the data, Section 3.2.4); and 0.72% of the data are flagged as outliers compared to the common-mode (Section 3.2.1).

The white noise levels of SCUBA-2 bolometers are measured between 2 and 10 Hz in the PSDs (as described in Section 3.2.5), leading to noise equivalent powers (NEPs, with units $\mathrm{W\,s^{1/2}}$) – the rms time-series noise in a 1 s integration (see section 3.5.2 in Holland et al. 2013). The NEPs are then converted into more useful noise equivalent flux densities (NEFDs, with units $\mathrm{Jy\,s^{1/2}}$) through multiplication by the extinction correction and the FCF. For an ideal scan pattern in which every bolometer spends an equal amount of time observing each point on the sky, the expected noise in a map pixel is $\mathrm{NEFD_{eff}}/t^{1/2}$, where t is the integration time, and the effective NEFD, $\mathrm{NEFD_{eff}} = (1/\sum \mathrm{NEFD}_i^{-2})^{1/2}$, is the sensitivity of the entire array including all bolometers i. Experimentally it has been found that the map noise based on the weighted scatter of the data (Eq. 5), and the scatter of map pixels in small apertures, both correlate well with this expected limiting noise performance for maps that are larger than the array footprint (for smaller maps the assumption of uniform coverage is incorrect). As an example of observing under favourable conditions with line-of-sight opacities of 0.87 and 0.34 at 450 and 850 µm (zenith sky opacities at 225 GHz of 0.04 and 0.065 at 450 and 850 µm, respectively, at an average airmass of 1.2, from table 3 in Holland et al. 2013), the mapping speed is approximately 6×10^{-5} and $3 \times 10^{-3}\,\mathrm{deg^2\,hr^{-1}\,mJy^{-2}}$, at 450 and 850µm, for the default pixel sizes of 2 and 4 arcsec, respectively. If maps are filtered and cross-correlated with the PSF for the optimal extraction of point sources (see Section 4.2), the mapping speeds increase to approximately 5×10^{-4} and $1.5 \times 10^{-2}\,\mathrm{deg^2\,hr^{-1}\,mJy^{-2}}$ in this example, independently of the chosen map pixel sizes. See the on-line SCUBA-2 integration time calculator for mapping speeds under arbitrary observing conditions and scan modes[5].

---

[5] http://www.jach.hawaii.edu/jac-bin/propscuba2itc.pl

4 EXAMPLES

While most of the steps described in Section 3 for reducing data with SMURF are applicable to all data sets, there is no "default" reduction that provides good results for a wide range of source S/N and angular scales. However, SMURF does have a small number of configurations with variations on these baseline parameters that are applicable to most common types of data. In this section we illustrate the differences between these configurations with the following examples: a bright point source, Uranus (Section 4.1); a blind survey of high-redshift galaxies in the Lockman Hole (Section 4.2); and a map of a bright extended star-forming region in our Galaxy, M17 (Section 4.3).

4.1 Known point source

The accurate measurement of positions and brightnesses of known point sources are necessary in real-time to establish telescope pointing offsets and focus. They are also necessary to measure the FCF (absolute calibration), and hence noise performance of the instrument in astronomically-useful units. In this example we reduce a 450 µm map of Uranus (observation 26 on 2011 October 17), which is a nearly point-like source for SCUBA-2 that is commonly used as a primary flux calibrator. The CV daisy pattern was used, with a scan speed of 155 arcsec sec^{-1}. We perform several different reductions of the data to illustrate the purpose of various model components and the convergence properties of the solution (Fig. 11). In all cases the maps are produced on a grid of azimuth (horizontal) and elevation (vertical) offsets from the position of Uranus (the origin), using 2 arcsec pixels.

The first, simplest reduction of the data uses only the `COM` model to estimate and remove the common-mode signal in order to suppress low-frequency noise in the data. After `COM`, the extinction correction is applied (`EXT`), and an initial map is estimated using equal weighting for all of the detectors. This estimate of `AST` is then removed from the data, and the noise is measured in the residuals to estimate weights for the subsequent and final iteration. The resulting map after these two iterations is shown in Fig. 11a. While the peak S/N of Uranus is clearly large (∼160), enabling us to see the faint sidelobes (circle and cross pattern), the map also has obvious circular streaks and other large-scale ripples. The circular streaks are due to the fact that `COM` does not account for all of the low-frequency (i.e., uncorrelated) noise (see Fig. 2), and therefore each bolometer leaves a trace of the circular scan pattern in the map, as their baselines slowly drift independently. A significant contribution to the larger-scale ripples in the map, however, can be made by degeneracies in the map solution, as we discuss below.

To illustrate how large-scale ripples can form (and grow), the same map solution is run for 100 iterations and shown in Fig. 11b, now exhibiting a strong vertical gradient. The degeneracy is easy to understand if the time-domain behaviour of each model component is considered. The top panel of Fig. 12 shows the residual signals for a single bolometer after 2 (black) and 100 (grey) iterations, which are nearly identical, yet the change in the estimated `COM`[6] (green) and `AST` (red) signals between 2 and 100 iterations are large However, it is also clear that the estimated `COM` and `AST` signals are complementary. In other words, the large change in the `AST` signal is cancelled by freedom in the `COM` signal to grow with opposite sign. For comparison, the bottom panel of Fig. 12 shows the telescope pointing for this section of data, and the shapes of the `AST` and `COM` signals match the elevation component, which is aligned with the gradient in Fig. 11b. Generically, the calculation of `COM` will remove any information on angular scales that are larger than the array footprint (outline shown in Fig. 11b for reference), meaning that the map solution is unconstrained on such large scales.

Attacking the problem of streaks, a simple method of removing residual (un-correlated) sources of low-frequency noise is to apply a high-pass filter after the common-mode removal. A third reduction of the data uses the baseline map-making parameters, as described in Section 3, which adds the `FLT` model to accomplish this task immediately prior to map estimation. We set the filter edge based on an angular scale of 200 arcsec, which, given the scan speed of 155 arcsec sec^{-1}, corresponds to a frequency of 0.78 Hz (note in Fig. 2 that this frequency is slightly above the $1/f$ knee at 450 µm after common-mode removal). Now using the automatic map-based convergence test (Section 3.3), the solution converges after 10 iterations (Fig. 11c). Both the circular streaks and the large-scale gradient are now removed, but they have been replaced by an obvious, circularly-symmetric ringing pattern about Uranus. The reason for this ringing is that the hard-edged high-pass filter in frequency space is equivalent to a sinc function-like response in map space. Since the scan pattern is fairly isotropic (scans at all position angles), and there is a bright point-like source at the centre, the result is an azimuthally-symmetric sinc function-like pattern in the map. The peak flux has also been attenuated to 0.353 pW in this reduction, compared with 0.358 pW in the first two reductions. The gradient resulting from the degeneracy between the common-mode and map has been removed because the filter scale of 200 arcsec (3.3 arcmin) is smaller than the array field-of-view (∼5 arcmin). If it were greater, degeneracies would again begin to appear on those larger scales.

This example illustrates the need for constraints in the map solution in many situations. For calibrators (and other previously known bright, compact sources), a good, simple prior is to constrain the map to a value of zero away from the known locations of emission (part of the `AST` model calculation, Section 3.2.4). In Fig. 11d, a solution is produced in an identical manner to Fig. 11c, but now setting the map explicitly to zero beyond a radius of 60 arcsec from the location of Uranus (much larger than the FWHM of the main lobe), for all but the final iteration. In this case, the map converges after 6 iterations, and the ringing has been effectively removed. The attenuation from the previous reduction is now removed, and Uranus again has a peak value of 0.358 pW. For reference, the Uranus model distributed with Starlink predicts a peak brightness of 176 Jy on this date, yielding an FCF of 491 Jy pW^{-1}, which is well within

---

[6] `COM` has been multiplied by the time-varying extinction correction to enable direct comparison with `AST`.

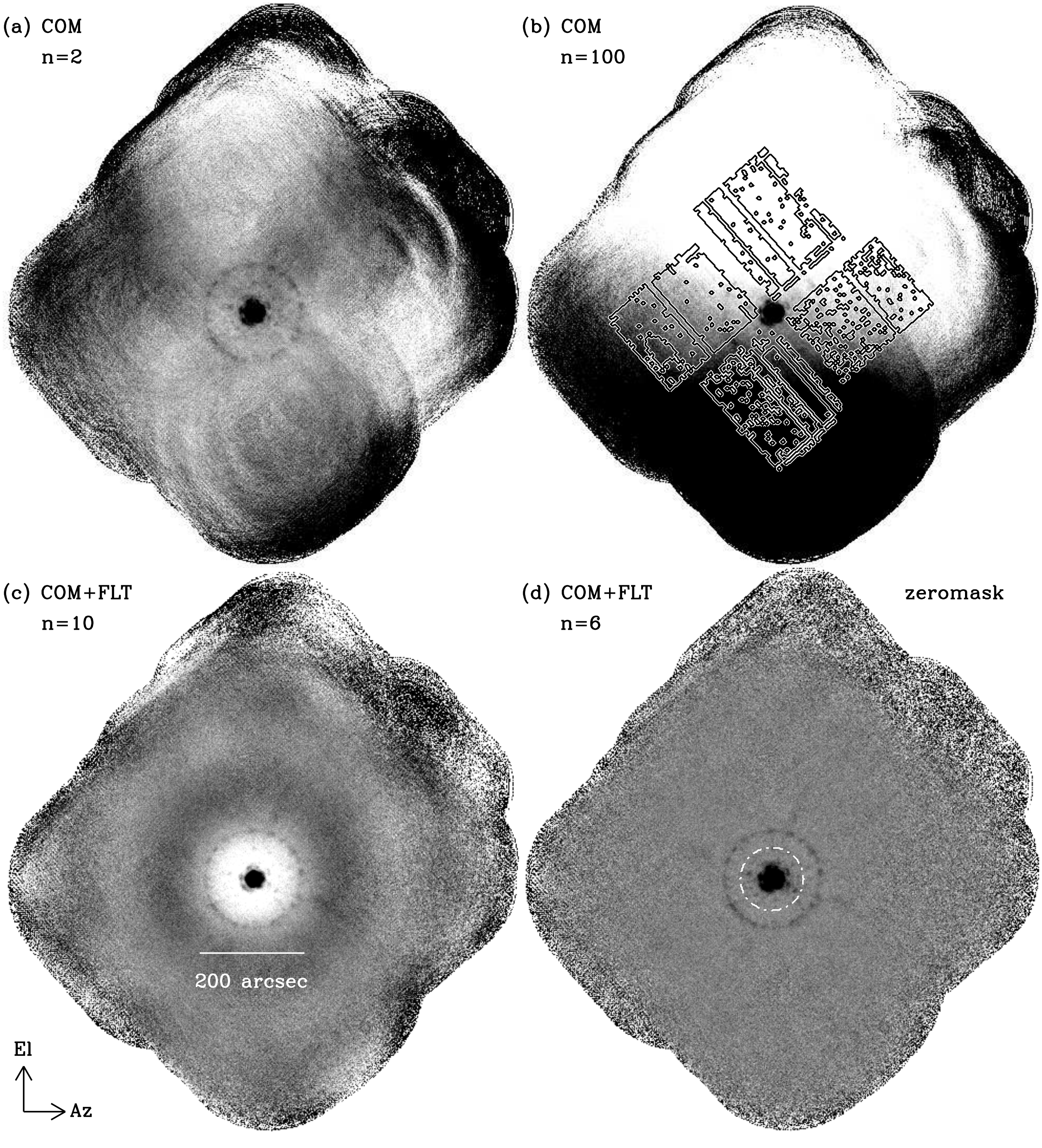

Figure 11. Multiple reductions of a 450 μm CV daisy scan of Uranus, all scaled between −0.002 pW (white) and +0.002 pW (black). In all cases extinction correction has been applied immediately after common-mode removal. (a) Reduction in which only common-mode subtraction is used to suppress low-frequency noise, and the reduction is forced to use 2 iterations (after the first iteration an estimate of the source flux is removed, and the noise is measured in the residuals to obtain appropriate weighting for the second and final iteration). Circular streaks are caused by independent low-frequency noise that is not removed by the common-mode (Uranus peak 0.358 pW). (b) Same as (a) but using 100 iterations, illustrating the degeneracy between large-scale structure and the common-mode (the footprint of working bolometers is also shown for reference, Uranus peak 0.358 pW). (c) Reduction in which high-pass filtering above 0.775 Hz (corresponding to a spatial scale of 200 arcsec, as indicated) is applied after common-mode removal, but before the map estimate. The map-based convergence test is activated and the solution halts after 10 iterations, but leaving large-scale ringing due to the filter (Uranus peak 0.353 pW). (d) Same as (c), but now the region of the map beyond the white dot-dashed circle is constrained to a value of zero until all but the final iteration. The map is now extremely flat, there is no attenuation of the source flux compared with the first two reductions, and the diffraction pattern is clearly seen (Uranus peak 0.358 pW).

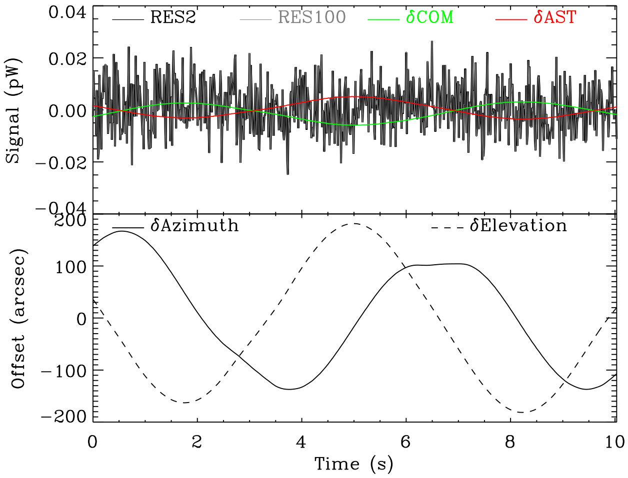

Figure 12. Demonstration of the degeneracy between large-scale structures in the map and common-mode removal, corresponding to panels (a) and (b) in Fig. 11. The black and grey lines in the top panel show the residual signal for a single bolometer after 2 and 100 iterations, respectively (they are nearly identical; the black line lies beneath the grey line). The green and red lines show the difference between the `COM` and `AST` (the signal produced by the current map estimate for a given bolometer) model components for that bolometer between iterations 2 and 100, respectively. This shows that a strong signal has grown over time, and it has equal but opposite signs in the two model components, so that they cancel one another. The bottom panel shows the scan pattern of the telescope over the same period; clearly the `COM/AST` model degeneracy is correlated with the elevation offset, and referring to Fig. 11, panel (b), this corresponds to the strong vertical gradient that has appeared

.

the typical range for SCUBA-2 of $(492 \pm 67)\,\mathrm{Jy\,pW^{-1}}$ (see Dempsey et al. 2013, for details). Since the map is now flat away from the source, and constrained to a value of zero, it is appropriate for performing aperture photometry directly, with no need for an additional reference annulus.

The way this prior works can be understood from the point of view of differential measurements. Bolometer data contain information up to scales corresponding to the filter edge (or the scale of the array footprint, whichever is smallest). In this example, the relevant scale is 200 arcsec. Since the map is constrained to zero within 60 arcsec of the peak of Uranus (well within 200 arcsec), the solution is able to accurately reconstruct the differential peak intensity of Uranus with respect to this constrained background. This approach to map-making is similar to that employed for poorly cross-linked scans of compact (though resolved) sources by Wiebe et al. (2009) using BLAST data.

4.2 Deep point source survey

SCUBA-2 surveys designed to detect extremely faint point-sources (e.g., high-redshift star-forming galaxies, and features in debris disks) are ideally limited by the white-noise performance of the instrument. The approach described here for maximising the S/N of point-sources involves three major steps: (i) generating a map that removes most large-scale noise sources with approximately linear response, without prior knowledge of the location of sources; (ii) apply a Fourier-space "whitening filter" to suppress residual large-scale noise; and (iii) detecting point sources using a "matched filter". Note that variations on this general procedure have been used extensively in the submm cosmology community using previous instruments (e.g., Scott et al. 2002; Borys et al. 2003; Laurent et al. 2005; Coppin et al. 2006; Scott et al. 2008; Perera et al. 2008; Devlin et al. 2009). In this section we reduce scans of the Lockman Hole taken during S2SRO as a pilot project for the SCUBA-2 Cosmology Legacy Survey. It consists of ~ 8.5 hours of data taken in 36 separate scans (average 15 min. each) spread over February and March 2010. Each scan is a 360 arcsec rotating PONG pattern, with a scan speed of $240\,\mathrm{arcsec\,s^{-1}}$, covering an area of about $50\,\mathrm{arcmin^2}$. The full list of dates and observation numbers includes: 2010 February 18, 63, 64, 65, 70, 71, 72, 90, 91, 92, 97, 98, 99; 2010 February 20, 111, 112, 113, 118, 128, 129, 130; 2010 March 3, 61, 62, 64, 69, 70, 72, 73, 74, 75; 2010 March 9, 87, 88, 90, 91; and 2010 March 11, 59, 64, 65, 72. These observations represent about 80 per cent of the total data taken as part of the project; the remaining observations were dropped due to problems in keeping the arrays properly tuned during S2SRO, and were easily identified by their highly variable and erratic bolometer time-series (which resulted in maps full of large streaks).

The first step, map generation, is different from that described in Section 4.1 in two key ways. Since the locations of sources are unknown *a priori*, a map constraint is not employed. Large-scale diverging structures in the map must be mitigated, and the method used in this example (the baseline processing in SMURF) is to apply a high-pass filter to the data once, as a pre-processing step. The iterative solution is then run using only `COM`, `EXT`, `AST`, and `NOI`. In other words, there is no information in the bolometer signals below some cutoff frequency, and residual correlated high-frequency noise above the cutoff is only removed through iterative common-mode subtraction. In this case, the filter edge has been chosen to remove scales larger than 200 arcsec, or a high-pass filter above 1.2 Hz given the scan speed. Since the data are high-pass filtered prior to the iterative solution, `GAI` (fitting an independent amplitude of `COM` to each bolometer) has been de-activated, since there is very little structure in the common-mode with which to fit an accurate gain. The map is shown in Fig. 13a. The map-maker has been tested in two ways: (i) large numbers of iterations are used to verify that the maps converge without the growth of large structure; and (ii) adding synthetic sources to the real time-series data (a built-in feature of SMURF) at a range of brightnesses verify that the map-maker response to them is linear (i.e., the relative shape and amplitude compared to the input source is independent of brightness). The response to a synthetic point source (solid line) after map-making (dotted line) is shown in Fig. 14. Clearly the use of a high-pass filter as a pre-processing step, and having no other map-constraints, has the down-side of introducing sidelobes around the main peak. Furthermore, the details of this shape depends on the high-pass filter edge that has been chosen (the higher the frequency, the greater the attenuation of the central peak, and the larger the negative side-lobes). However, the way this filter affects point-sources is measurable (using the synthetic source injection facility of SMURF), and linear.

Even though the map looks quite flat, there is a mixture

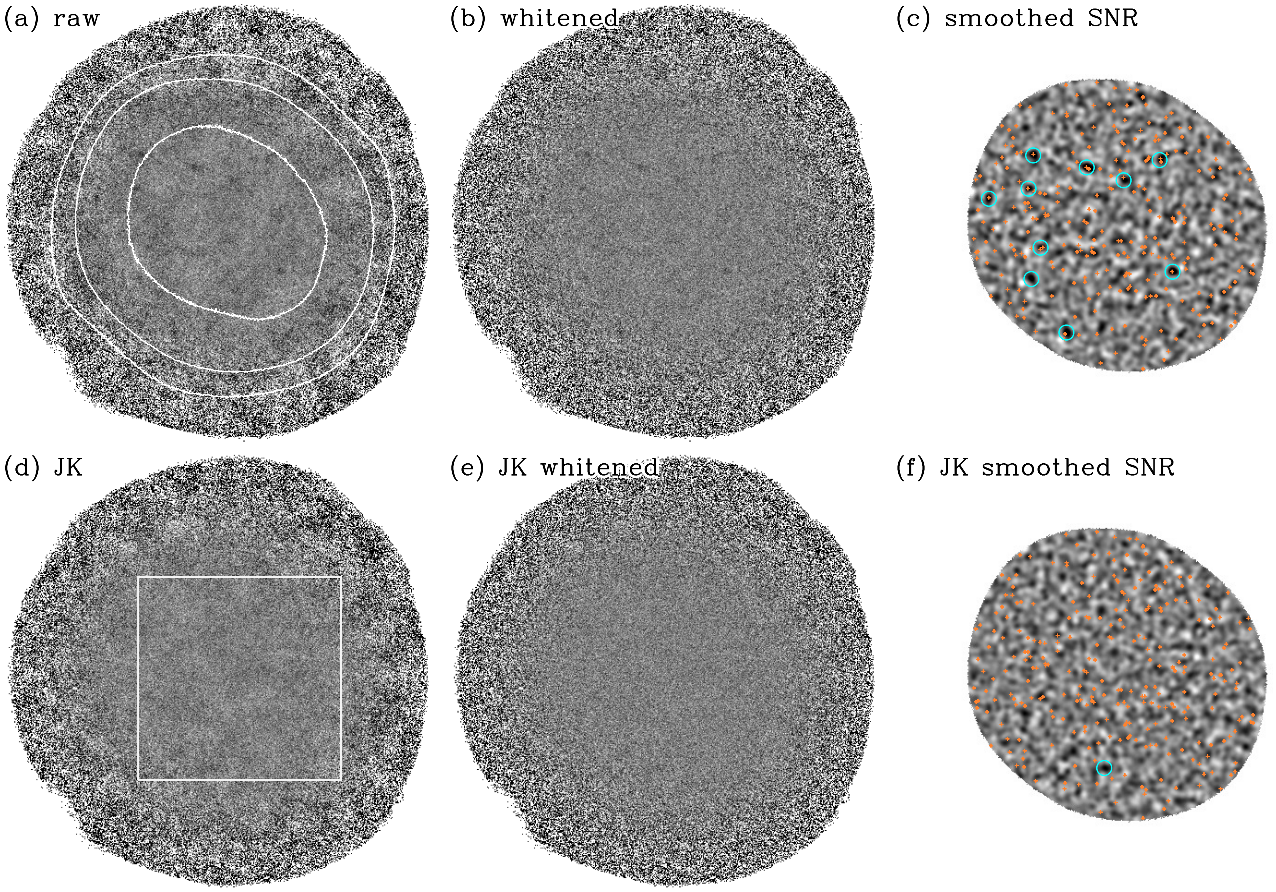

Figure 13. Reduction of a blank-field survey: the Lockman Hole. (a) Raw output of SMURF using high-pass filtering as a pre-processing step, followed by 4 iterations using only the `COM` model to remove residual correlated noise. White contours correspond to estimated noise levels of 1.25, 2.5 and 5.0 times the minimum noise at the centre of the map. (b) The whitened map using a filter based on the angular power spectrum of the jackknife map. (c) The whitened map cross-correlated with the whitened PSF to identify point sources [restricted to a lower-noise region, within the area denoted by the second contour of panel (a)]. The image shows the S/N with 3.8-σ peaks indicated by blue circles (radius 8 arcsec). The orange "+" signs show the locations of 1.4 GHz radio sources from Owen & Morrison (2008) with $S \gtrsim 15\,\mu$Jy. Of the 10 submm peaks, 9 are within a search radius of 8 arcsec of at least one radio source. (d) Jackknife map produced from the difference of two maps, using the even and odd scan numbers, respectively. Provided that all noise sources are statistically uncorrelated between the two halves of the data, the map is a plausible realisation of the noise without contamination from astronomical sources. (e) The jackknife map whitened using the same filter as that in panel (b). The whitened jackknife map cross-correlated with the same whitened PSF as in panel (c). Again, orange "+" and blue circles indicate radio sources and 3.8-σ peaks, respectively. Unlike panel (c), there is only a single (apparently) significant peak, and it is not in the vicinity of a radio source.

of faint astronomical sources, and what is probably residual low-frequency noise, causing faint patchiness visible to the naked eye. Since the mixture of the two components is unknown, the first step is to suppress the low-frequency noise, under the assumption that such contaminants occur randomly in time, while astronomical sources are (usually) constant.

First, the angular power spectrum of noise is estimated from a "jackknife map": maps are produced from two independent halves of the total data set, and the jackknife signal in a map pixel, $S_{\rm JK}$, and its variance, $\sigma^2_{\rm JK}$ are estimated from the two input map fluxes, S_1, S_2, and the corresponding variances, σ^2_1, and σ^2_2 as,

$$S_{\rm JK} = \frac{S_1 - S_2}{2}, \qquad (10)$$

$$\sigma^2_{\rm JK} = \frac{\sigma^2_1 + \sigma^2_2}{4}. \qquad (11)$$

Provided that the noise in one half of the data is uncorrelated with that from the other half, the signal in the jackknife map should resemble noise drawn from the same parent distribution as that of the real map. The astronomical signal, however, should be cleanly removed (provided that there are no strong time-varying signals, and also assuming that errors due to calibration between the two halves are insignificant). The approach we have taken to minimize systematics is to produce the two maps using odd and even scan numbers (i.e., each map will contain a nearly uniformly-spaced sampling of data across the full data set).

Since the SCUBA-2 scan strategy is usually isotropic (all position angles scanned with roughly equal weights), we make the simplifying assumption that the angular noise power spectrum is azimuthally symmetric. For these data, there are no obvious anisotropic structures in the 2-dimensional FFT. The radial (azimuthally-averaged) angu-

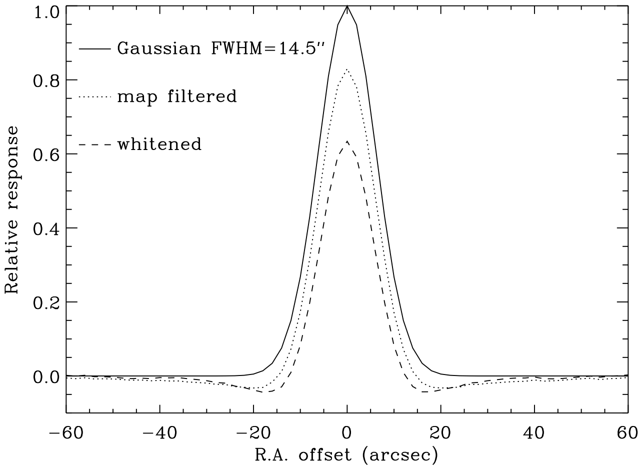

Figure 14. Slice through the angular response to an ideal Gaussian point source (solid line) along the R.A. axis following map-making using the blank-field processing configuration with SMURF (dotted line), and upon application of the whitening filter (dashed line). The "map filtered" response is produced by adding the ideal Gaussian to the real data near the centre of the Lockman Hole map, and re-reducing the data. The resulting dotted line gives the expected shape of a source in panel (a) from Fig. 13. Applying the whitening filter to the dotted line (dividing the Fourier Transform of the map filtered response by the square root of the solid orange line in Fig. 15, and then transforming back to real space) gives the whitened line (dashed), which is the expected shape of a source in panel (b) from Fig. 13. Finally, cross-correlating the whitened map with this whitened PSF is an effective "matched filter" for identifying point-like sources, and this smoothed map is shown in panel (c) of Fig. 13.

lar power spectrum therefore encodes all of the useful information about the noise properties. These power spectra for the raw output of SMURF, and the jackknife map (transforming only the approximately uniform region indicated by the square in Fig. 13d in each case) are shown by the dashed black, and solid orange lines in Fig. 15, respectively. Both power spectra are approximately flat at spatial frequencies $\gtrsim 0.06\,\mathrm{arcsec}^{-1}$ (scales $\lesssim 16$ arcsec), with the exception of a spike at $\sim 0.175\,\mathrm{arcsec}^{-1}$ (a scale of ~ 5.7 arcsec). One possibility for this feature is that it is related to the inter-bolometer spacing in the focal plane (which happens to be this size): small relative drifts in the baselines of adjacent bolometers may produce faint parallel stripes in the map along the scan direction (the superposition of many scans at different angles then results in an isotropic noise pattern). It is not likely that this signal is due to astronomical sources because it appears with a nearly equal amplitude in both the real map and the jackknife. At lower spatial frequencies, both the real map and the jackknife power spectra grow significantly, as a result of the more obvious large-scale patchiness in Figs. 13(a) and (d).

To suppress noise in the map, we construct a whitening filter whereby the Fourier Transform of the map is divided by the square root of the jackknife power spectrum (orange line in Fig. 15), normalised by the white-noise level estimated from the RMS power at angular frequencies $> 0.1\,\mathrm{arcsec}^{-1}$, and transforming back into real space. The whitened map is shown in Fig. 13b, and for comparison, the jackknife map has also been whitened in Fig. 13e. In both cases, the maps are visibly flatter than the non-whitened cases.

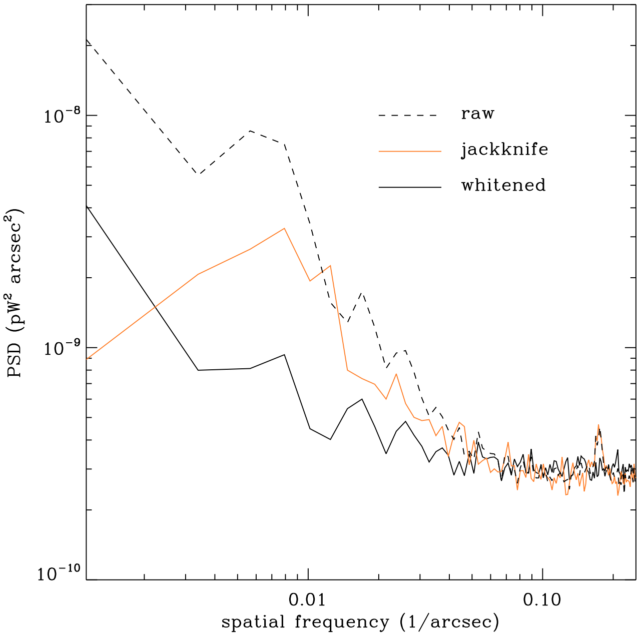

Figure 15. Radial (azimuthally-averaged) angular power spectral densities for the raw map output by SMURF (dashed black line), the jackknife (solid orange line), and whitened (solid black line) maps (panels (a), (d), and (b) from Fig. 13, respectively), considering only the square region indicated in Fig. 13d. Since the raw map contains spatially correlated signals on large scales, both due to noise and astronomical signals (low-spatial frequencies), the jackknife map (difference of two approximately equal-length subsets of the data) is used to generate a plausible realisation of pure noise. Assuming that the noise properties are isotropic, a whitening filter is estimated from the reciprocal of the jackknife power spectrum with only a radial dependence. The power spectrum of the resulting signal map still has residual power on large scales, which is presumably due to astronomical sources.

The angular power spectrum of the whitened signal map is shown with a solid line in Fig. 15. At low angular frequencies ($\lesssim 0.5\,\mathrm{arcsec}^{-1}$) there is significantly less power than for the raw map. However, it also clearly has some power in excess of the white noise level. In theory, this residual signal is produced by astronomical sources, although its origin cannot be determined from this plot alone; nor are astronomical sources readily visible in the map (Fig. 13b). To identify sources, we next apply a "matched filter" to the whitened maps.

For blind, high-redshift surveys, individual sources are expected to be un-resolved by the SCUBA-2 7.5–14.5 arcsec FWHM beams. Under this assumption, and also assuming that the map noise is white, cross-correlation between the map and the known PSF, or matched filtering, yields the maximum-likelihood flux density of supposed point-sources centred over every location in the resulting map (an extremely well-known result throughout astronomy, see Stetson 1987). Peak identification in such smoothed maps have been used extensively in the submillimetre community, as both an efficient source-detection and photometric measurement strategy. For the case at hand, we may use this cross-correlation technique since the map has been whitened.

However, we must first establish the effective shape of point sources in this map due both to map-making itself, and the whitening filter. We determine the effect of map-making by adding a synthetic (and high-S/N) point source to the real data, and measure its resulting shape in the map (solid and dotted lines in Fig. 14, respectively). Next, the Fourier Transform of the map filtered PSF is divided by the square root of the jackknife noise power spectrum to calculate the final whitened PSF (dashed line in Fig. 14). Both the whitened signal and jackknife maps are smoothed by this shape and shown in Figs. 13c and f, respectively. Note that these images are plotted in S/N units, where the smoothed noise maps have been calculated by propagating the original noise maps output by SMURF through both the whitening and matched filters (each of which is a linear operations). In terms of the angular power spectra, this complete process can be thought of as an optimal band-pass filter that has both suppressed low-frequency noise, and information on scales that are smaller (higher frequencies) than the beam.

Have real astronomical sources been detected using the matched filter? For both the smoothed signal and jackknife maps, blue circles denote 3.8-σ peaks. While not justified here, this threshold is fairly typical for other ground-based submillimetre surveys in recent years (e.g., Coppin et al. 2006; Perera et al. 2008; Weiß et al. 2009) leading to estimated false-identification rates of order ∼5%, and is chosen as a convenient reference. In the former, 10 peaks are found, whereas there is only 1 in the latter. However, this test does not preclude the possibility that some correlated noise made it into the jackknife map, in which case the estimated S/Ns are misleading.

One simple test of the calculated noise properties is to compare the signal and jackknife S/N distributions with ideal Gaussians. The top panel of Fig. 16 shows the whitened (but not match-filtered) signal (blue) and jackknife (histograms), along with a Gaussian (mean 0, standard deviation 1, and area normalised to the number of map pixels) as a dashed line. In this case, it is clear that the S/N distributions for both maps are nearly indistinguishable from the theoretical distribution of white noise. This result shows us that: (i) the whitening filter appears to have removed correlated large-scale noise, since the jackknife map histogram is consistent with white noise; and (ii) any potential astronomical signals are small compared to the typical white noise in most map pixels (unsurprising given the appearance of Fig. 13b). Next, we examine the S/N histograms for maps processed with the matched filter in the bottom panel of Fig. 16. Again, the histogram of the jackknife S/N data appears consistent with pure noise. However, the signal map now deviates significantly from a Gaussian distribution, with a clear positive tail (as one would expect for emitting sources). In fact, integrating the positive tails beyond our 3.8-σ source-detection threshold (vertical solid line) yields 229 map pixels in the signal map, compared with 3 in the jackknife map (out of 80603 pixels in the entire region). Recall that given the small pixel size of the map, several pixels generally contribute to each peak. This procedure gives only a flavour of the analysis that is usually required to produce a robust source lists. Additional tests, along with a careful consideration of completeness and false-positive rates, usually require a series of Monte Carlo simulations that are beyond the scope of this work. We direct the interested reader to a selection of papers on the subject: Scott et al. (2002); Coppin et al. (2006); Perera et al. (2008); Weiß et al. (2009) and Chapin et al. (2011).

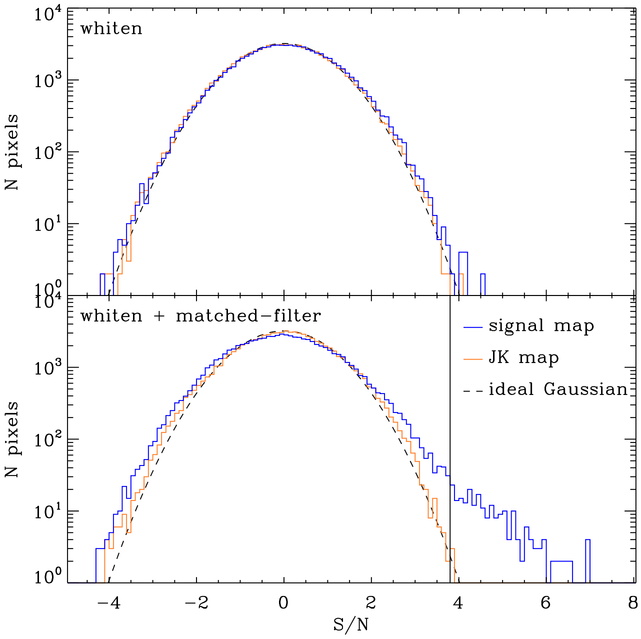

Figure 16. Histograms of S/N using pixels from the central region of the Lockman Hole (second contour) in Fig. 13a. The top panel shows the histograms for pixels from the whitened signal and jackknife maps (Figs. 13b,e), compared to a Gaussian distribution with mean zero, standard deviation one, and an area normalised to the total number of pixels – the expected distribution for a map of spatially-uncorrelated Gaussian noise. The good agreement indicates that these maps are indeed dominated by white noise. The lower panel shows the results for matched filtered signal and jackknife maps (Figs. 13c,f). The filtered jackknife map distribution is still close to the expectation (Gaussian), but now the matched filter has picked out significant signal, leading to the large positive tail. The vertical solid line shows the chosen 3.8-σ source-detection threshold.

As an additional external check, we have over-plotted orange "+" signs at the locations of 1.4 GHz radio sources from Owen & Morrison (2008) with $S \gtrsim 15\,\mu$Jy. Such radio catalogues have historically proven invaluable for the precise identifications of high-redshift submillimetre galaxies due to their low surface densities (compared with optical catalogues, for example), and a strong correlation between the radio and submillimetre emission mechanisms (e.g., Smail et al. 2000; Pope et al. 2006; Ivison et al. 2007; Chapin et al. 2009). Taking a representative search radius of 8 arcsec from these studies with similar S/N sources and source sizes (the same size as the blue circles), 9 out of 10 peaks in the smoothed signal map have potential radio counterparts, whereas the single peak in the smoothed jackknife map does not lie near any radio source. Again, a proper cross-identification analysis must inevitably include simulations to establish completeness, false-positive rates, as well as the effects of point source clustering and confusion. See the aforementioned papers and references therein for examples.

For future, significantly deeper SCUBA-2 maps, in which the RMS in a PSF-smoothed map is dominated by

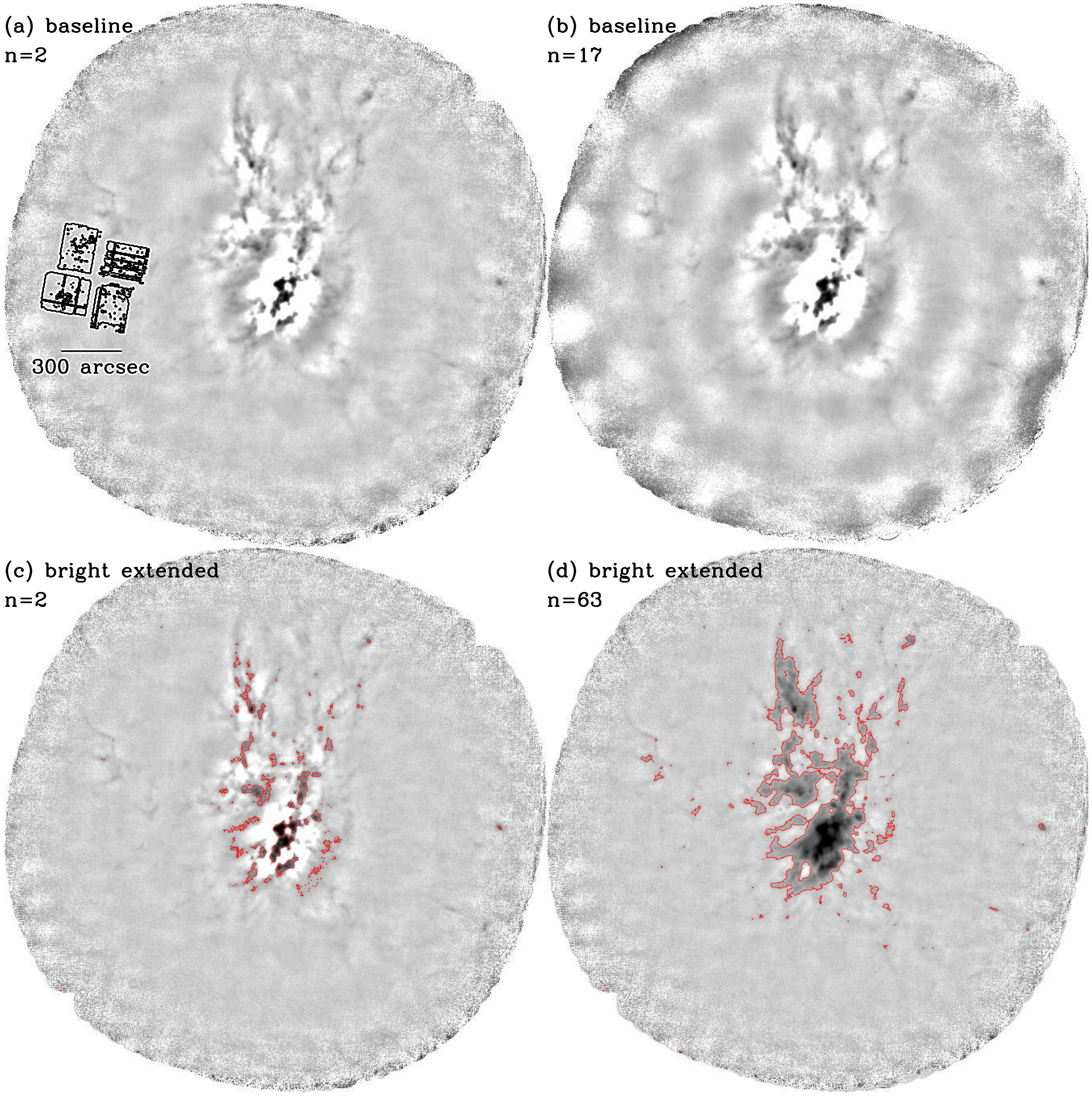

Figure 17. An 850 µm rotating PONG map of M17. Intensity is logarithmically scaled between −0.0003 pW (white) and +0.01 pW (black). Iteration numbers are given in the corner of each panel. Panels (a) and (b) show the results for a reduction using the baseline parameters (the solution halted after reaching the map-based convergence criterion in 17 iterations). Panel (a) also depicts the array footprint (position angle indicative of the start of the observation), and a 300 arcsec line shows the spatial scale corresponding to the `FLT` high-pass filter. Similar to Fig. 11c, the high-pass filtering introduces ringing around bright sources. Panels (c) and (d) show the "bright extended" reduction, in which a zero-mask is created iteratively from all of the pixels that lie below a S/N of 5. While this region (outside the red contour) only avoids the brightest peaks early in the solution, in the final iteration it skirts most of the bright, extended emission, and significantly helps with negative ringing.

point-source confusion, rather than instrumental noise, a modified matched filter will offer improved results. See Appendix A in Chapin et al. (2011), which shows how to include confusion (when known *a priori*) explicitly as a noise term in the calculation of such filters.

4.3 Bright extended emission

In this final example, we analyse a map of M17 which contains bright, extended emission. The data are from observation 11 on 2011 May 31 using the 850 µm array. It is a rotating PONG scan covering a diameter of 0.375 deg, with a scan speed of 300 arcsec s^{-1}, and a transverse spacing of 180 arcsec, taking 37.5 min to complete.

The baseline reduction of these data is shown in the top panels of Fig. 17, after 2 iterations (the first map estimated after the noise weights have been measured) and 17 iterations (when the map has converged), which uses iterative common-mode subtraction and high-pass filtering. The first panel also depicts the array footprint, and the angular scale (300 arcsec) corresponding to the high-pass filter edge (0.6 Hz). Much like the reduction of a point source without any prior constraints (Fig. 11c), there are ripples around bright sources due to the filtering.

Unlike the case of a known point-source (Section 4.1), it may not be possible for the observer to define, in advance, a mask of regions containing blank sky. Indeed, for this map, much of the field clearly contains extended structure. Furthermore, the goal of such maps may be to detect previously unknown cool, dense regions of the ISM that may not have appeared at other wavelengths (e.g., the first optically-thick cloud-collapse stages of star-formation). While the option does exist for the user to supply their own mask, a facility has been added to SMURF to generate one automatically by flagging pixels below some S/N threshold to be set to zero after each iteration as part of the "bright extended" configuration.

The results of this automatic masking are shown in the bottom panels of Fig. 17. After the second iteration, everything but the brightest peaks are set to zero (outside the red contours). However, as the solution progresses, the negative bowls around the bright sources are slowly reduced and the mask "grows" out from the brightest areas. By the final iteration, most of the obvious structures in the data are excluded in the mask, negative bowling is significantly reduced, and the brightest regions are more extended.

While the reduction in the bottom panels of Fig. 17 is (in a cosmetic sense) superior to those in the top panels, it is important to quantify both the noise properties of the maps, and the response to real structures (the transfer function). We would also like to know how each are affected by our choice of filter scale. Similar to the previous section, we will use a jackknife test to estimate the noise, as well as injecting known sources into the data to observe how they are attenuated.

Maps are produced using the first and second continuous halves of the data in Fig. 18. This is not an ideal situation, since the noise properties may evolve with time (e.g., due to changing sky conditions), leading to a biased estimate of the parent noise distribution in the complete map from the jackknife. Also, since the zero-masking depends on the S/N of the map, it will be restricted to regions approximately $\sqrt{2}$ times shallower in these maps than for the full data set. Finally, the cross-linking (position angles sampled) is similar, though not identical in the two halves. Ideally one would have many full maps, as in the case of the Lockman Hole data in the previous section, from which alternating maps could be combined.

Since our goal in this section is to measure the response of the map-maker to extended structures, we inject a simulated signal with power at a range of scales into a relatively empty region of the map. It is created by drawing a realisation of noise from an angular power spectrum $P(k) \propto k^{-3}$, which is appropriate for Galactic cirrus clouds (e.g., Gautier et al. 1992), within an 800 arcsec on-a-side box. It is then filtered again with a 14.5 arcsec Gaussian to model the effect of the SCUBA-2 optical response. The RMS of these fluctuations is then normalised to 0.002 pW so that they are comparable to the dynamic range of M17 itself. The minimum is then subtracted so that the signal is positive. Finally, multiplication by half a period of a (1+cosine)/2 function is used to roll-off the signal to zero between radii of 300 and 400 arcsec.

The first row of Fig. 18 shows the total signal image averaging the maps made of each independent half of the data, for the baseline configuration (inverse-variance weighting has been used). The columns show reductions using 150, 300, 600, and 900 arcsec filter edges. The synthetic data are clearly seen as the circular region south of M17. As the filter scale is increased, the size of the ripples increases accordingly. While larger astronomical structures do seem to appear, negative bowls are a major problem without any other map constraints. Since the largest scale that is completely inscribed by the array footprint is about 400 arcsec, and the diagonal of the array is about 600 arcsec, scales ranging from ∼400–600 arcsec up to the scale of the filter will be unconstrained due to the degeneracy between the common-mode and map (see discussion in Section 4.1). This degeneracy therefore causes some of the large-scale patchiness in the 600 and 900 arcsec filtered maps that lie away from the central bright sources. The second row of Fig. 18 shows the jackknife maps. The astronomical emission is almost perfectly removed, except for a slight impression of M17 near the centre of the map, which is probably due to some combination of detector gain and pointing drifts. Otherwise the jackknife appears to be a plausible realisation of noise from the same parent distribution as for the averaged maps.

The third and fourth rows in Fig. 18 repeat this exercise using the bright extended configuration, in which the S/N threshold of 5 is again used to identify low-significance pixels that are set to zero after each iteration. As the filter scale is increased, more of the extended structure in M17 is reproduced in the map, as evidenced by the blue and red contours (masks generated from the first and second halves of the data, respectively). The masking does a generally good job of suppressing the largest-scale ripples that are produced by the baseline reduction. However, the noise away from regions of bright emission does increase noticeably (mottled appearance) — due to residual $1/f$ noise following common-mode removal that has a knee at a frequency above the filter edge. With filter scales $\gtrsim$ 600 arcsec, virtually the entire region of synthetic emission is correctly identified by the S/N mask and allowed to vary freely in the solution.

Next, we analyse the angular power spectral densities (PSDs) of the maps to understand the signal and noise properties of the map-maker in the region of synthetic sources, as a function of filter scale. In Fig. 19a we show the raw PSDs for the input synthetic signal (thick black line), the output map signals (thin solid lines), and the jackknife maps (dashed lines). Colours encode the filter scales used: 150 arcsec (red); 300 arcsec (orange); 600 arcsec (green); and 900 arcsec (blue). Note that, with the exception of the synthetic data, we only plot the PSDs down to the second-lowest spatial frequency bin of 1.875×10^{-3} arcsec^{-1}, or 533 arcsec, since the lowest is very poorly sampled, and therefore noisy. At small scales ($\lesssim$20 arcsec) the map and jackknife PSDs

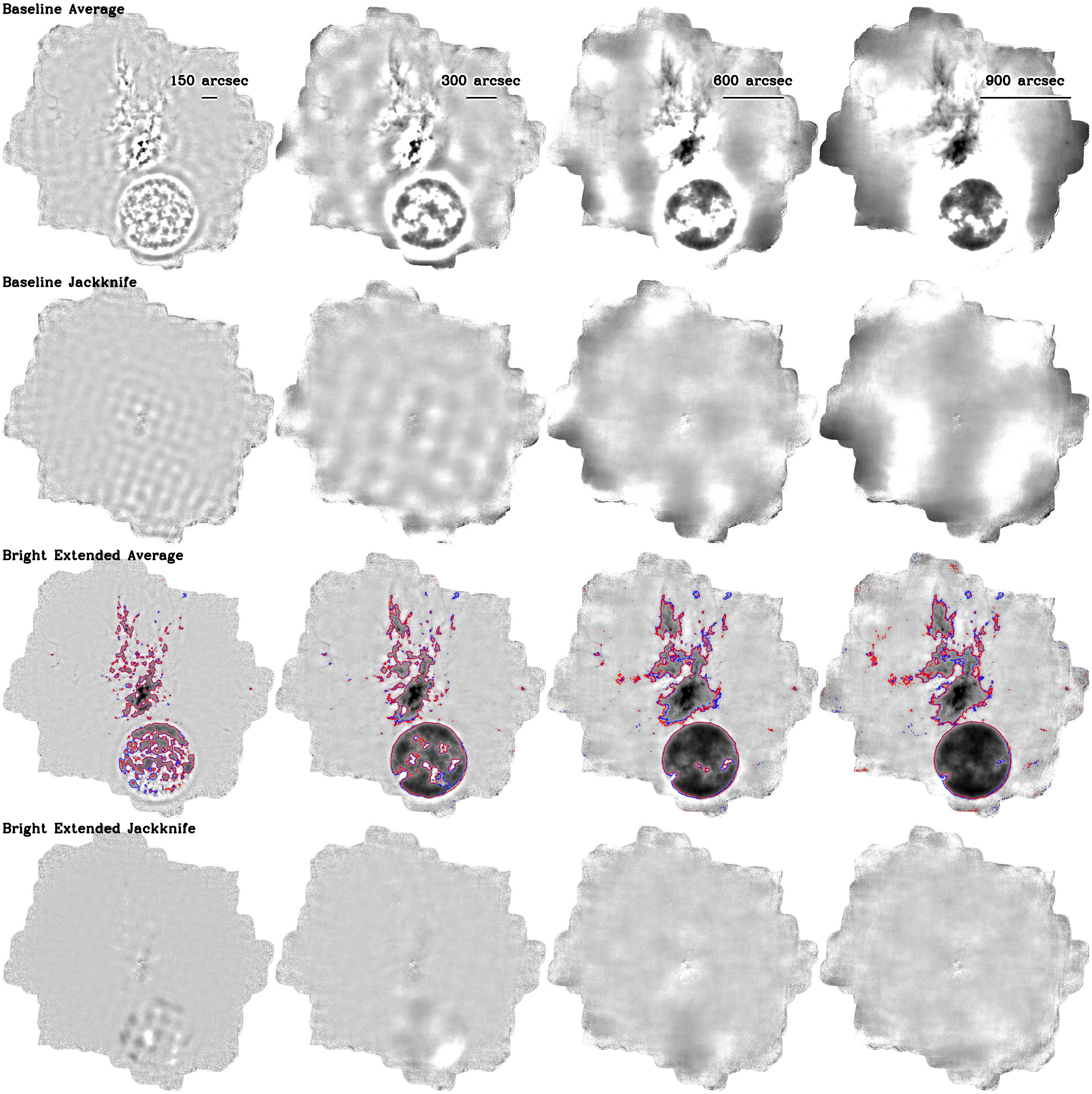

Figure 18. Maps of M17 used to characterise the noise properties and transfer function of SMURF (same intensity scale as Fig. 17). For each column, a different high-pass filter edge scale was adopted (indicated in the top panels). First (top) row: average of two halves of the data analysed independently, using the baseline configuration. The data have had added to them synthetic signal within a 600 arcsec diameter circle (south of M17) created as a realisation of noise from a $P(k) \propto k^{-3}$ angular power spectrum multiplied by the PSF, subtracting the minimum to make it positive, scaling it to a similar signal range as M17 itself, and rolling-off the edges smoothly using half a period of a radial (1+cosine)/2 function across 100 arcsec beyond the edge of the 600 arcsec region. Second row: jackknife maps produced from the differences of the maps of each half of the data that went into the first row. Third row: average of the two halves of the data using the bright extended reduction. The regions outside the blue and red contours are constrained to zero for each half of the data (note for the 300 arcsec case that these regions about M17 closely match the mask in Fig. 17d using a full reduction). Clearly as the filter scale is increased, due to the high S/N of the data, larger emission regions are (correctly) detected and reproduced in the map. Fourth (bottom) row: Jackknife maps for the bright extended reductions.

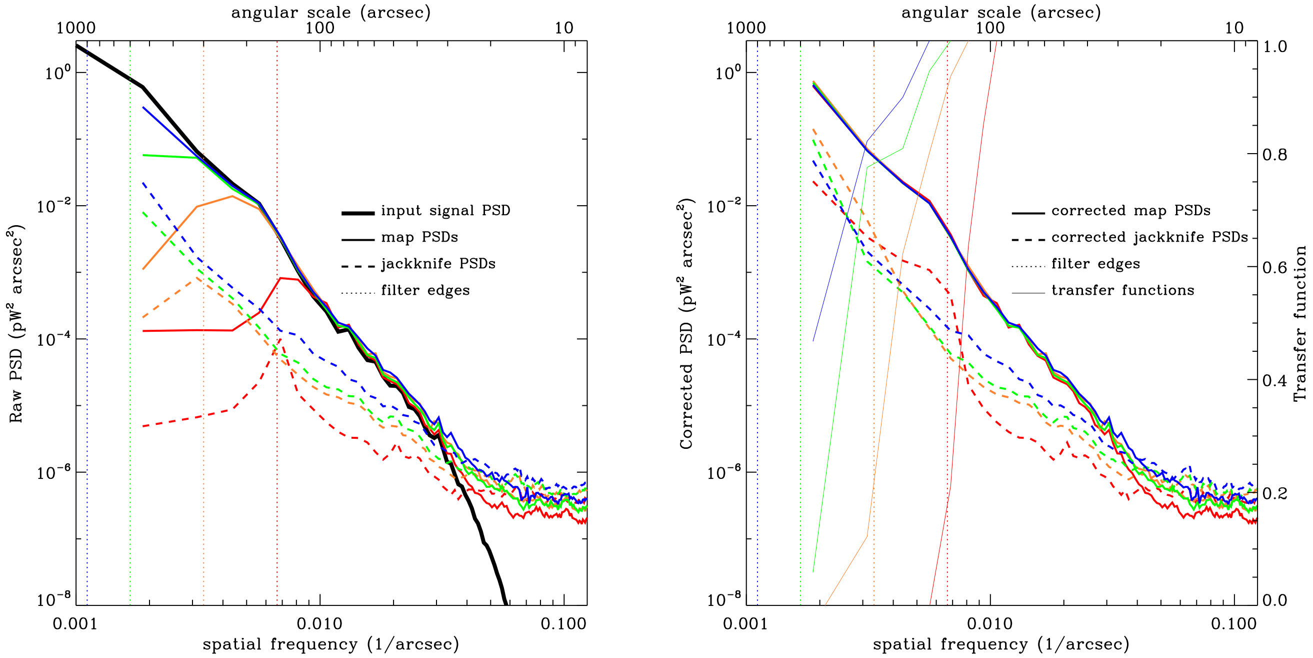
(a) baseline reduction PSD

(b) baseline reduction transfer function

Figure 19. Angular PSDs for the region of the M17 map in Fig. 18 containing synthetic data, using the baseline configuration. (a) Raw PSDs for the input (noiseless) simulated data (thick black line), the signal (average of each half) PSDs (thin solid lines), and noise PSDs estimated from the jackknives (dashed lines). Vertical dotted lines indicate the high-pass filter scales: 150 arcsec (red); 300 arcsec (orange); 600 arcsec (green); and 900 arcsec (blue). PSDs are also colour-coded by filter scale. (b) Since the input PSD is known, it is possible to measure the transfer function of the map-maker as the ratio between the difference of the output map signal PSDs and jackknife PSDs, and the input PSDs, giving the thin coloured lines (linear vertical axis shown on right of plot). The remaining lines are as in (a), but now corrected by the transfer function. This plot shows that increasing the filter scale improves the S/N at intermediate scales (∼200–600 arcsec), although the S/N worsens at smaller scales ($\lesssim$200 arcsec).

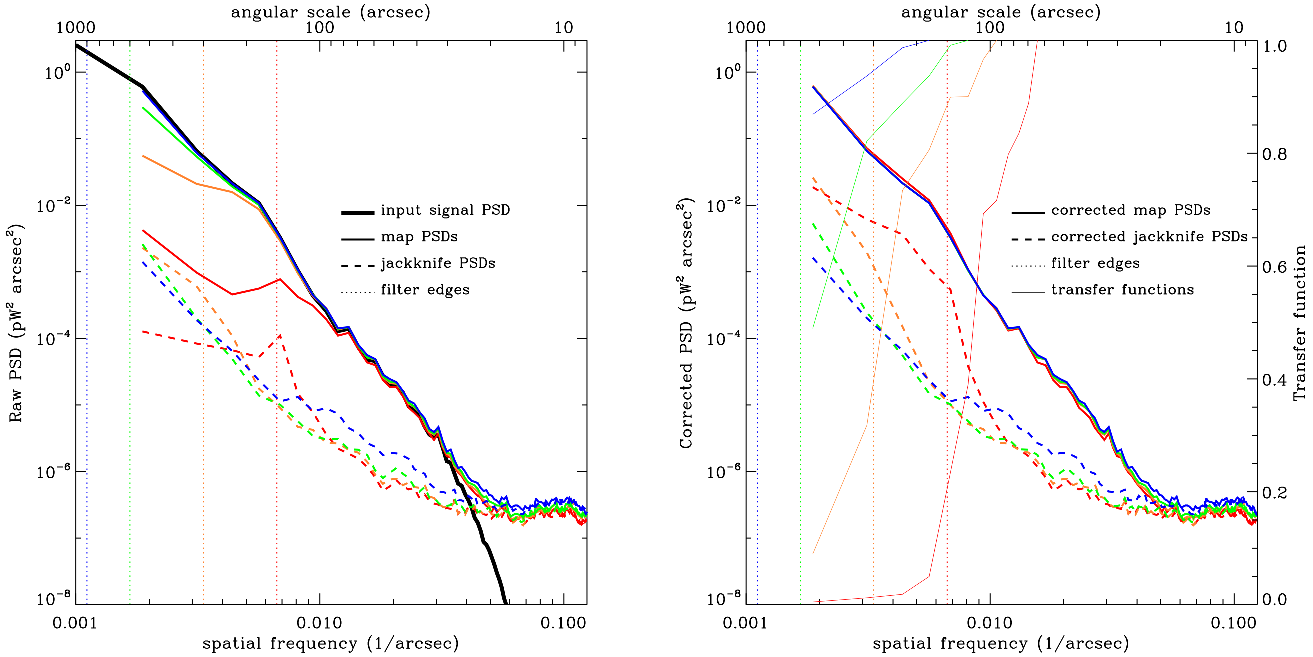
(a) bright extended reduction PSD

(b) bright extended reduction transfer function

Figure 20. Lines have same meaning as in Fig. 19, except now using the bright extended configuration. This configuration has resulted in an improved transfer function and S/N at large angular scales. Also note that increasing the filter scale does not have as large an impact on the small-scale noise as in the baseline configuration.

flatten. However, unlike Fig. 15, these white noise levels are slightly larger in the jackknife maps, suggesting that the differences have not completely removed the astronomical signals. A strong possibility is that the two half-maps that go into the differences have not converged equally, probably due to the lack of prior constraints. As the filter edge is increased, more power is measured in the map PSDs at larger scales. However, much of this power is clearly produced by noise which appears in the jackknife PSDs. We estimate the map-maker transfer function as the ratio between the portion of the signal PSDs not produced by noise, to the input PSD, or

$$G(k) = \frac{P_{\mathrm{M}}(k) - P_{\mathrm{JK}}(k)}{P_{\mathrm{S}}(k)}, \qquad (12)$$

where k is the spatial frequency, and the subscripts "M", "JK", and "S" refer to the signal map, jackknife map, and synthetic map, respectively.

The transfer functions $G(k)$ are plotted as thin solid lines in Fig. 19b. This formula produces extremely noisy values at large frequencies (small scales), and we therefore set it to a value of 1 above 0.015 arcsec^{-1}, as well as any point in the curve where $P_{\mathrm{M}}(k)$ exceeds $P_{\mathrm{S}}(k)$ [i.e., $G(k)$ is assumed to be $\leqslant$1]. As expected, the larger the scale of the filter, the lower the spatial frequency at which the map transfer function falls. We then correct the map and jackknife PSDs by dividing by $G(k)$ to produce the thick solid, and dashed lines in Fig. 19b. This shows us that, even though the raw noise in Fig. 19a is lower at small scales when a smaller-scale filter is used (e.g., the red dashed line), once we correct for the transfer function, we actually win in a S/N sense at large scales using the larger-scale filter (the corrected noise is lower), as would be expected.

These tests are then repeated using the bright extended reduction, in Fig. 20. The most obvious improvement with this reduction over the baseline reduction is that the transfer functions fall more slowly at large angular scales, accompanied by a slower increase in noise; in other words, there is greatly improved S/N at large angular scales (an obvious conclusion given the appearance of the maps in Fig. 18). In fact, using the 900 arcsec filter edge, the map response is still above 80 per cent right out to the largest scale accurately measured in the PSDs, 533 arcsec, which is about the largest scale that should be recoverable, given the size of the array footprint and the fact that we use common-mode rejection. Another interesting feature of these reductions is that the increase in small-scale noise as the filter edge is increased is not as drastic as in the baseline reduction. Finally, note that both the map and jackknife white noise levels (at scales $\lesssim$20 arcsec) are in excellent agreement, unlike the previous example.

One case in which the S/N is worse using the bright extended reduction is when using a 150 arcsec filter. Here the noise is considerably larger in the bright extended reduction, as evidenced by the "kink" near 150 arcsec. Referring to the mask contours in the left panel of the third row in Fig, 18, it is clear that the map-maker has failed to identify much of the bright, extended emission in the region of the synthetic source. Each area that is not within the contours is constrained to zero throughout the solution, therefore suppressing power (and lowering the transfer function), and subsequently reducing the S/N of the final result. This measurement serves as a warning: the map-maker response is non-linear when using S/N masking. Harsh filtering can provide misleading results, as in this example. Maps of faint extended emission will also suffer considerably, as the structures of interest may lie below the S/N threshold for the mask.

Note that alternatives to the zero-masking approach do exist for other iterative map-makers. For example, Kovács (2008a) typically restricts the solution to a small fixed number of iterations ($\lesssim$10), so that there is probably little opportunity for degeneracies between the map and common-mode to appear in the map. Experimentation with the model order is also advocated to gain an impression of the convergence properties. This approach is perhaps more relevant to their SHARC-2 data for which a more complicated model is developed; the degeneracies we have observed for SCUBA-2 maps using our more brute-force approach with a high-pass filter tend to look similar regardless of the order (only the convergence time is affected). For Bolocam data of the Galactic Plane, Aguirre et al. (2011) used a maximum-entropy filtering step to suppress large-scales. Regardless of the method used, simulations are always required to establish the transfer function and noise properties as a function of angular scale.

5 CONCLUSIONS

This paper has described the Submillimetre User Reduction Facility (SMURF), which was designed to produce maps from the rapidly sampled $\sim 10^4$ bolometers of the SCUBA-2 instrument. While similar to other algorithms in the literature that iteratively model and remove correlated noise components from the data, successively improving the map (e.g., Kovács 2008a; Aguirre et al. 2011; Schuller 2012), we have shown that a fairly simple approach provides good results for SCUBA-2 data, with reasonable computational requirements. This conclusion is encouraging for the development of future large-format bolometer arrays, for which our specific approach should be useful when even larger volumes of data are involved.

A major obstacle to making maps of SCUBA-2 data is low-frequency correlated noise (probably a mixture of atmospheric signals and magnetic field pickup), which occurs at predominantly $\lesssim$2 Hz. Much of this signal can be removed using common-mode rejection, although principal component analysis (PCA) identifies a number of other less-significant correlated noise patterns at low frequencies. Unfortunately these patterns are difficult to model, and their character varies from observation to observation. One could use the PCA directly to remove them, but this technique is prohibitively slow for existing high-end desktop computers, given the volume of SCUBA-2 data. However, we have demonstrated that high-pass filtering can remove the bulk of these residual correlated noise components using significantly more efficient Fast Fourier Transforms (FFTs). The basic algorithm therefore consists of iterative common-mode rejection and high-pass filtering along with estimates of the map, which allows us to approach the white-noise limit of the instrument.

We have found that the iterative solution tends to diverge on large angular scales due to the degeneracy between the map, and the low-frequency signal components that are removed (namely the common-mode). In addition, the high-pass filtering produces significant ringing around bright sources. A simple strategy of constraining empty regions of the map to zero (using either a user-supplied mask for known sources, or an iterative determination of signal below some S/N threshold) provides good constraints for both compact objects, and bright/extended structures. Particularly in the latter case, using a combination of synthetic sources and an empirical measurement of the map noise from jackknife tests (differences of independent portions of the data), we have demonstrated that we can effectively recover angular scales up to the order of the array footprint (approximately 5 arcmin).

For maps of faint point-sources, a single (non-iterative) high-pass filter at the start of the reduction produces maps that are nearly white-noise limited and linear (i.e., the response does not depend on S/N). Residual large-scale noise can be removed with a whitening filter (also established from jackknife estimates of the noise) based on the Fourier Transform of the maps, and sources detected using a matched-filter (smoothing with the effective filtered point spread function).

The iterative solution is stopped once convergence in the map itself is achieved. This enables SMURF to run in a pipeline setting without user interaction for a wide variety of observations. Furthermore, the execution times are typically shorter than the observation lengths, and memory requirements for even the longest SCUBA-2 observations are within the capabilities of single, high-end desktop computers. SMURF can therefore provide real-time feedback at the telescope to observers.

One regime in which SMURF does not presently perform well is in maps of faint extended structures, since the zero-masking technique we have adopted cannot be used. Since SMURF is both highly configurable and extensible, it may be possible to develop an improved data model and/or map constraint to assist in these situations, as more experience with the instrument is gained. However, provided sufficient computing power is available, the best solution in the long-term will be a maximum-likelihood algorithm, such as SANEPIC (Patanchon et al. 2008). Even in this case, the existing iterative solution from SMURF will probably be used as an initial step, since it can quickly clean the bolometer time-series, as well as perform map-based despiking (a necessarily iterative procedure).

6 ACKNOWLEDGEMENTS

The James Clerk Maxwell Telescope is operated by the Joint Astronomy Centre on behalf of the Science and Technology Facilities Council of the United Kingdom, the Netherlands Organisation for Scientific Research, and the National Research Council of Canada. Additional funds for the construction of SCUBA-2 were provided by the Canada Foundation for Innovation. This research used the facilities of the Canadian Astronomy Data Centre operated by the National Research Council of Canada with the support of the Canadian Space Agency. This research was supported in part by the Natural Sciences and Engineering Research Council of Canada. EC thanks CANARIE/CANFAR for additional funding. The authors thank the members of the SCUBA-2 commissioning team for testing the map-maker and reporting anomalies; in particular Antonio Chrysostomou and Jessica Dempsey. We also thank Mark Halpern, Matthew Hasselfield, and Gaelen Marsden for many useful discussions; observers who provided helpful feedback, especially David Nutter and Todd McKenzie; and Mandana Amiri and Dan Bintley for consultations regarding the SCUBA-2 Multi-Channel Electronics. We acknowledge the contributions of Dennis Kelly, Alex van Engelen and Jennifer Balfour for early investigations related to SMURF; and Mark Thompson, Craig Walther and Séverin Gaudet for being on the Critical Design Review panel. We thank Per Friberg and Gary Davis for their helpful comments on the manuscript. Finally, we thank the anonymous referee for their thorough review that helped to clarify several key areas of the paper.

REFERENCES

Aguirre J. E. et al., 2011, ApJS, 192, 4
Battistelli E. S. et al., 2008, Journal of Low Temperature Physics, 151, 908
Borys C. et al., 2004, MNRAS, 352, 759
Borys C., Chapman S., Halpern M., Scott D., 2003, MNRAS, 344, 385
Carlstrom J. E. et al., 2011, PASP, 123, 568
Cavanagh B., Jenness T., Economou F., Currie M. J., 2008, Astronomische Nachrichten, 329, 295
Chapin E., Hughes D. H., Kelly B. D., Holland W. S., 2002, in de Petris M., Gervasi M., eds, American Institute of Physics Conference Series Vol. 616, Experimental Cosmology at Millimetre Wavelengths. pp 357–359
Chapin E. L. et al., 2011, MNRAS, 411, 505
Chapin E. L. et al., 2009, MNRAS, 398, 1793
Coppin K. et al., 2006, MNRAS, 372, 1621
Das S. et al., 2011, ApJ, 729, 62
Dempsey J. T. et al., 2013, MNRAS, 430, 2534
Devlin M. J. et al., 2009, Nat, 458, 737
Economou F. et al., 2011, in Evans I. N., Accomazzi A., Mink D. J., Rots A. H., eds, ASP Conf. Ser. Vol. 442, Astronomical Data Analysis Software and Systems XX. Astron. Soc. Pac., San Francisco, p. 203
Fowler J. W. et al., 2010, ApJ, 722, 1148
Gautier III T. N., Boulanger F., Perault M., Puget J. L., 1992, A J, 103, 1313
Gibb A. G., Scott D., Jenness T., Economou F., Kelly B. D., Holland W. S., 2005, in Shopbell P., Britton M., Ebert R., eds, ASP Conf. Ser. Vol. 347, Astronomical Data Analysis Software and Systems XIV. Astron. Soc. Pac., San Francisco, p. 585
Glenn J. et al., 1998, in Phillips T. G., ed., Proc. SPIE Vol. 3357, Advanced Technology MMW, Radio, and Terahertz Telescopes. SPIE, Bellingham, p. 326
Holland W. S. et al., 2013, MNRAS, 430, 2513
Ivison R. J. et al., 2007, MNRAS, 380, 199
Janssen M. A., Gulkis S., 1992, in M. Signore & C. Dupraz ed., NATO ASIC Proc. 359: The Infrared and Submillimetre Sky after COBE. Kluwer Academic Publishers, Dordrecht, p. 391
Jenness T., Berry D. S., Cavanagh B., Currie M. J., Draper P. W., Economou F., 2009, in Bohlender D. A., Durand

D., Dowler P., eds, ASP Conf. Ser. Vol. 411, Astronomical Data Analysis Software and Systems XVIII. Astron. Soc. Pac., San Francisco, p. 418

Jenness T., Economou F., 1999, in Mehringer D. M., Plante R. L., Roberts D. A., eds, ASP Conf. Ser. Vol. 172, Astronomical Data Analysis Software and Systems VIII. Astron. Soc. Pac., San Francisco, p. 171

Jenness T., Economou F., 2011, in Telescopes from Afar. (arXiv:1111.5855). Canada-France-Hawaii Telescope

Jenness T., Holland W. S., Chapin E., Lightfoot J. F., Duncan W. D., 2000, in Manset N., Veillet C., Crabtree D., eds, ASP Conf. Ser. Vol. 216, Astronomical Data Analysis Software and Systems IX. Astron. Soc. Pac., San Francisco, p. 559

Jenness T., Lightfoot J. F., 1998, in Albrecht R., Hook R. N., Bushouse H. A., eds, ASP Conf. Ser. Vol. 145, Astronomical Data Analysis Software and Systems VII. Astron. Soc. Pac., San Francisco, p. 216

Johnstone D., Wilson C. D., Moriarty-Schieven G., Giannakopoulou-Creighton J., Gregersen E., 2000, ApJS, 131, 505

Kackley R., Scott D., Chapin E., Friberg P., 2010, in Radziwill N. M., Bridger A., eds, Proc. SPIE Vol. 7740, Software and Cyberinfrastructure for Astronomy. SPIE, Bellingham, p. 77401Z

Kovács A., 2008a, in Duncan W. D., Holland W. S., Withington S., Zmuidzinas J., eds, Proc. SPIE Vol. 7020, Millimeter and Submillimeter Detectors and Instrumentation for Astronomy IV. SPIE, Bellingham, p. 70201S

Kovács A., 2008b, in Duncan W. D., Holland W. S., Withington S., Zmuidzinas J., eds, Proc. SPIE Vol. 7020, Millimeter and Submillimeter Detectors and Instrumentation for Astronomy IV. SPIE, Bellingham, p. 702007

Laurent G. T. et al., 2005, ApJ, 623, 742

Omont A., Cox P., Bertoldi F., McMahon R. G., Carilli C., Isaak K. G., 2001, A&A, 374, 371

Owen F. N., Morrison G. E., 2008, A J, 136, 1889

Patanchon G. et al., 2008, ApJ, 681, 708

Perera T. A. et al., 2008, MNRAS, 391, 1227

Pope A. et al., 2006, MNRAS, 370, 1185

Sayers J. et al., 2010, ApJ, 708, 1674

Schaffer K. K. et al., 2011, ApJ, 743, 90

Schuller F., 2012, in Holland W. S., Zmuidzinas J., eds, Proc. SPIE Vol. 8452, Millimeter, Submillimeter, and Far-Infrared Detectors and Instrumentation for Astronomy VI. SPIE, Bellingham, pp 8451T–1

Scott K. S. et al., 2008, MNRAS, 385, 2225

Scott S. E. et al., 2002, MNRAS, 331, 817

Smail I., Ivison R. J., Owen F. N., Blain A. W., Kneib J., 2000, ApJ, 528, 612

Stetson P. B., 1987, PASP, 99, 191

Stompor R. et al., 2002, PhRvD, 65, 022003

Swetz D. S. et al., 2011, ApJS, 194, 41

Tegmark M., 1997, ApJL, 480, L87

Warren-Smith R. F., Wallace P. T., 1993, in Hanisch R. J., Brissenden R. J. V., Barnes J., eds, ASP Conf. Ser. Vol. 52, Astronomical Data Analysis Software and Systems II. p. 229

Weferling B., Reichertz L. A., Schmid-Burgk J., Kreysa E., 2002, A&A, 383, 1088

Weiß A. et al., 2009, ApJ, 707, 1201

West D. H. D., 1979, CACM, 22, 532

Wiebe D. V. et al., 2009, ApJ, 707, 1809

Wilson G. W. et al., 2008, MNRAS, 386, 807

Wright E. L., Hinshaw G., Bennett C. L., 1996, ApJL, 458, L53